

Sensitivity of a Cloud-Resolving Simulation of the Genesis of a Mesoscale Convective System to Horizontal Heterogeneities in Soil Moisture Initialization

WILLIAM Y. Y. CHENG AND WILLIAM R. COTTON

Department of Atmospheric Science, Colorado State University, Fort Collins, Colorado

(Manuscript received 18 August 2002, in final form 17 March 2004)

ABSTRACT

This study examines the sensitivity of varying the horizontal heterogeneities of the soil moisture initialization (SMI) in the cloud-resolving grid of a real-data simulation of a midlatitude mesoscale convective system (MCS) during its genesis phase. The quasi-stationary MCS of this study formed in the Texas/Oklahoma panhandle with a lifetime of 9 h (2200 UTC 26 July to 0700 UTC 27 July 1998). Soil moisture for the finest nested grid (the cloud-resolving grid) was derived from the antecedent precipitation index (API) using 4-km-grid-spacing precipitation data for a 3-month period. In order to vary the heterogeneities of the SMI in the cloud-resolving grid, (i) Barnes objective analysis was used to alter the resolution of the soil moisture initialization, (ii) the amplitudes of the soil moisture anomalies were reduced, (iii) the position of a soil moisture anomaly was altered, and (iv) two experiments with homogeneous SMI (31% and 50% saturation) were performed. Because of the severe drought in the Texas/Oklahoma panhandle area, the saturation API value was lowered in order to introduce heterogeneities in the soil moisture for the sensitivity experiments.

All of the experiments with heterogeneous SMI (in addition to an experiment with a homogeneous SMI at 31% saturation) produced an MCS with a quasi-circular cloud shield, similar to the observed timing, size, and location. The authors' findings suggest that a soil moisture dataset with approximately 40-km grid spacing may be adequate to initialize a cloud-resolving model for simulating MCSs. For the simulations in this study, the soil moisture distribution determined where convection was likely to occur. Wetter soil tended to suppress convection for this case, and convection preferentially occurred around the peripheries of wet soil moisture anomalies.

1. Introduction

The interaction between the earth's surface and the overlying atmosphere is a major cause of cumulus convection (Pielke 2001). One important boundary condition in the land surface is soil moisture. Soil moisture, next to sea surface temperature (SST), is the second most important factor in increasing the predictability of the atmosphere (Dirmeyer and Shukla 1993; Dirmeyer 1995). Deep soil moisture has a memory on the time scale of 200–300 days (Liu and Avissar 1999; Pielke et al. 1999). According to J. Shukla (cited in Dirmeyer 1995), as a boundary condition, soil moisture may perhaps be more important than SST over the extratropical continents in the spring and summer. Soil moisture is also an important component of the hydrological cycle (Dirmeyer and Shukla 1993). In addition, initial soil moisture is known to have an impact on climate simulations (Pielke et al. 1999) and medium-range forecasts (Yang et al. 1994), as well as short-term simulations,

for example, 48 h or less (Bernardet et al. 2000; Natchamkin and Cotton 2000). Soil moisture affects the soil heat capacity and shortwave albedo of the surface (Entekhabi et al. 1996). In addition, soil moisture has a strong influence on the partitioning of surface latent and sensible heat fluxes, boundary layer evolution, and convective stability (Pielke 2001).

a. Nonclassical mesoscale circulations

Surface heterogeneities in vegetation type, soil type, or soil moisture can induce mesoscale circulations through surface sensible heat flux gradients (Segal and Arritt 1992). These surface sensible heat flux gradients result from spatial variations in surface evapotranspiration, solar irradiance reflection/absorption, and thermal energy storage of the surface. Pielke and Segal (1986) identified these thermally induced circulations as nonclassical mesoscale circulations (NCMCs). These NCMCs, much like sea-breeze-induced circulations, can provide regions of convergence, triggering deep convection (Pielke 2001).

Segal et al. (1988) examined the effects of vegetation and irrigated crops on mesoscale circulations in an idealized modeling study. Using both observations and an

Corresponding author address: William Y. Y. Cheng, Meteorology Department, and NOAA Cooperative Institute for Regional Prediction, University of Utah, Salt Lake City, UT 84112-0110.
E-mail: wcheng@met.utah.edu

idealized model, Segal et al. (1989) investigated the effects of irrigated crop areas on NCMCs. Pielke et al. (1997) performed sensitivity experiments to test the importance of landscape on thunderstorm development in the Texas/Oklahoma region. In one simulation, they used the current landscape (irrigated crops, shrubs, and natural short-grass prairie) and produced deep convection. In the second experiment, they used the natural landscape (short-grass prairie) but produced only shallow convection.

Chen and Avissar (1994a) investigated the impact of spatial variation of land surface wetness on mesoscale heat fluxes. They found that the strongest mesoscale heat fluxes occur for surface forcings with wavelengths corresponding to the local Rossby radius of deformation (80–130 km). Research by Dalu et al. (1991) and Dalu and Pielke (1993) also found similar results with surface thermal inhomogeneities in their idealized models. In a follow-up study dealing with shallow convection, Chen and Avissar (1994b) found that the most intense precipitation (for shallow convection) occurs when the wavelength of the land surface moisture discontinuity is close to the local Rossby radius (80–140 km). Even when the length scale of the land surface moisture discontinuity is on the order of 20 km, the induced mesoscale circulations can still produce heavy precipitation. In a 2D idealized model, Yan and Anthes (1988) placed strips of dry and moist land adjacent to each other in a convectively unstable environment. However, their results differ from those of Chen and Avissar (1994b). Yan and Anthes (1988) found that strips of 100–200 km (24 and 48 km) in width are (are not) effective in initiating convective precipitation. It is possible that the coarse grid spacing (ranging from 6 to 768 km in their stretched grid) in Yan and Anthes's model affected their results. On the other hand, Chen and Avissar (1994a) and Chen and Avissar (1994b) used a uniform grid spacing of 10 and 0.5 km, respectively.

b. Mesoscale convective systems

Mesoscale convective systems (MCSs) are a special class of convective system with horizontal length scales ranging from 20 to 500 km. Considerable research has been published on MCSs from observational studies (e.g., Maddox 1980; Cotton et al. 1983; Wetzel et al. 1983; Johnson and Hamilton 1988; Cotton et al. 1989) and modeling studies (e.g., Zhang et al. 1989; Olsson and Cotton 1997; Bernardet and Cotton 1998; Nachamkin and Cotton 2000). MCSs contain organized convective circulations on the mesoscale that are distinct from the circulations of the individual convective cells and the synoptic-scale circulation in which the mesoscale circulations are embedded (Zipser 1982). From satellite imagery, MCSs appear as large cold cirrus cloud shields (Maddox 1980). MCSs are ubiquitous; they can be found in the Tropics as well as the midlatitudes. MCSs account for a large percentage (30%–70%)

of summer rainfall in the central United States (Fritsch et al. 1986). In addition, MCSs such as squall lines and mesoscale convective complexes are associated with a large portion of severe weather during the spring and summer, especially flood-producing storms (e.g., Midwest floods of 1993; Kunkel et al. 1994; Bell and Janowiak 1995). On the other hand, too few MCSs in the central United States lead to drought. Hence, MCSs are important from a climatological and weather-forecasting perspective.

c. Motivation for this study

Currently, accurate high-resolution soil moisture data is unavailable to initialize models with large domains, such as those in numerical weather prediction models (Chen et al. 2001a). One major reason for this is the high cost of building a conventional network. The highest resolution of soil moisture measured from a conventional network is the Oklahoma Mesonet, with an average station spacing of approximately 50 km (<http://okmesonet.ocs.ou.edu>). The Oklahoma Mesonet measures soil moisture at four levels below ground: (i) 5, (ii) 25, (iii) 60, and (iv) 75 cm. As of now, remote sensing (low-frequency microwave) may offer the best hope in retrieving high-resolution soil moisture over a large domain. However, low-frequency microwave remote sensors have difficulties in retrieving soil moisture beyond the first few centimeters of the soil (Entekhabi et al. 1996; Njoku and Entekhabi 1996).

Past modeling studies have demonstrated the sensitivity of convection to soil moisture, but many of them were initialized with idealized atmospheric conditions. Also, few studies have examined the sensitivity of convective storm simulations to soil moisture on the cloud-resolving scale¹ with realistic heterogeneous initial atmospheric conditions, except for Grasso (2000), Ashby et al. (2001), and Chen et al. (2001b). Finally, even fewer studies have investigated the sensitivity of soil moisture initialization in cloud-resolving simulations of MCSs. Currently, many academic institutions, for example, Colorado State University, are already running their real-time forecast models at cloud-resolving scales. With the affordability of computing resources, seasonal simulations with regional models can be nested down to the cloud-resolving scale. Besides forecasting and climate studies, understanding the impact of soil moisture on convective systems has applications in agriculture and water resource management. Thus, it would be of value to test the impact of soil moisture initialization in cloud-resolving simulations of MCSs.

Since soil moisture is not measured on a routine basis, at 10-km grid spacing or less, an important question to address is, To what extent are MCSs sensitive to the finescale heterogeneities in soil moisture in a realistic

¹ We refer to cloud-resolving scale as horizontal grid spacing of 4 km or less (Weisman et al. 1997).

simulation? Since the results of Yan and Anthes (1988) and Chen and Avissar (1994b) differ in their conclusion as to whether smaller soil moisture anomalies are important in initiating convective precipitation, it is relevant to address the question of whether the NCMCs from smaller soil moisture anomalies (i.e., tens of kilometers in scale) are important in initiating convective precipitation. Emori (1998) found a negative soil moisture–convective precipitation feedback in his 2D simulations; that is, convective precipitation preferentially occurs over drier soil. Could this result still be applicable in 3D when an MCS is developing “upscale” from ordinary convective cells? How do the NCMCs generated by the soil moisture anomalies influence the development of MCSs?

To address the above issues, we simulated a typical MCS case in the central United States using real-data initialization. We examined the model’s sensitivity to (i) different degrees of heterogeneities in the soil moisture initialization (SMI), (ii) the amount of soil moisture, and (iii) the locations of soil moisture anomalies. Because of the severe drought in the Texas/Oklahoma panhandle area, we needed to adjust the saturation antecedent precipitation index in order to introduce heterogeneities in the soil moisture distribution (discussed in the appendix) in the sensitivity experiments. We wish to emphasize that we were not trying to replicate the event to 100% accuracy, but only to study sensitivity of the cloud-resolving MCS simulation to the SMI. By running real-data simulations, we can see how a model with realistic initial atmospheric conditions responds to different SMI, and how the NCMCs generated by the soil moisture anomalies influence the development of the MCS. Although easy to interpret, idealized simulations, often homogeneous, require artificial triggering mechanisms (warm bubble or cold pool) to initiate convection. However, artificial triggers (such as warm bubble or cold pool) do not realistically capture the genesis of MCSs. MCSs develop “upscale” from ordinary convective cells (McAnelly et al. 1997), but often synoptic and mesoscale features such as frontal boundaries, dry-lines, upper- and low-level jets provide a favorable environment for midlatitude MCSs to develop (Cotton and Anthes 1989). These features are often difficult to represent in idealized simulations. Therefore, we need to use real-data initialization in our MCS simulations in this study.

2. 26 July MCS case

The quasi-stationary MCS of interest initiated in the Texas/Oklahoma border near a quasi-stationary front (shown later) around 2200 UTC 26 July (26/2200 hereafter) and dissipated at approximately 0700 UTC 27 July 1998. Figure 1a shows the infrared (IR) satellite imagery at 26/1846. A small area of deep convection had occurred in the western Texas panhandle (A_1); A_1 was initiated when the outflow of the convection in New

Mexico encountered the quasi-stationary front in the Texas/Oklahoma panhandle. A shallow line of clouds (A_2), in a southwest–northeast orientation, developed along a surface trough that spanned across Oklahoma and Texas. By 26/1945 (Fig. 1b), convection in A_1 had intensified and deep convection along A_2 would develop shortly. By 26/2145 (Fig. 1c), A_1 had developed into an area of deep convection in the western Texas/Oklahoma panhandle region. Meanwhile, A_2 , advancing northward, intensified as it encountered the quasi-stationary front in the Texas panhandle region. By 27/0053 (Fig. 1d), A_1 and A_2 had merged into a common cloud shield, and the MCS had fully developed, covering the Texas/Oklahoma panhandle region and small parts of Colorado, New Mexico, and Kansas.

3. Model setup/initialization

We used the Colorado State University Regional Atmospheric Modeling System (RAMS) Version 4.29 (Cotton et al. 2003). Some key features of the model include: (i) the interactive Land Ecosystem–Atmosphere Feedback Model, version 2 (LEAF-2; Walko et al. 2000), (ii) a two-moment bulk microphysics package (Harrington et al. 1995; Meyers et al. 1997), and (iii) a two-stream radiative transfer model coupled to the microphysics package (Harrington 1997; Harrington et al. 1999). LEAF-2 prognoses the temperature and water content of soil, snow cover (nonexistent for this study), vegetation, and canopy air. In addition, LEAF-2 also considers the turbulent and radiative fluxes (i) among the above-mentioned components and (ii) between the atmosphere and the above-mentioned components. In addition, LEAF-2 contains a hydrological model that accounts for the surface and subsurface downslope lateral transport of groundwater. An additional feature of LEAF-2 allows the surface grid area to be divided into multiple subgrid areas or “patches” of distinct land types such that each patch possesses its own surface characteristics. Each patch interacts with the overlying atmosphere with a weight proportional to its fractional area. We used four land patches in this study, with land surface characteristics selected from the four most dominant land types for each grid area. The use of mosaic physiography may be unnecessary for the finest grid at 2.5-km horizontal grid spacing, but its use did not impose much additional computational resources. The two-moment microphysics package prognoses the number concentrations and mixing ratios of rain, pristine ice, aggregates, snow, graupel, and hail. The cloud water mixing ratio is prognosed, while the cloud water number concentration is specified. Water vapor mixing ratio is diagnosed. In addition, through the coupling with the two-moment cloud microphysics, the two-stream radiation model accounts for the habit (the nonsphericity) of the ice hydrometeors in the radiative transfer equations (Harrington 1997; Harrington et al. 1999).

No convective parameterization was used in any of

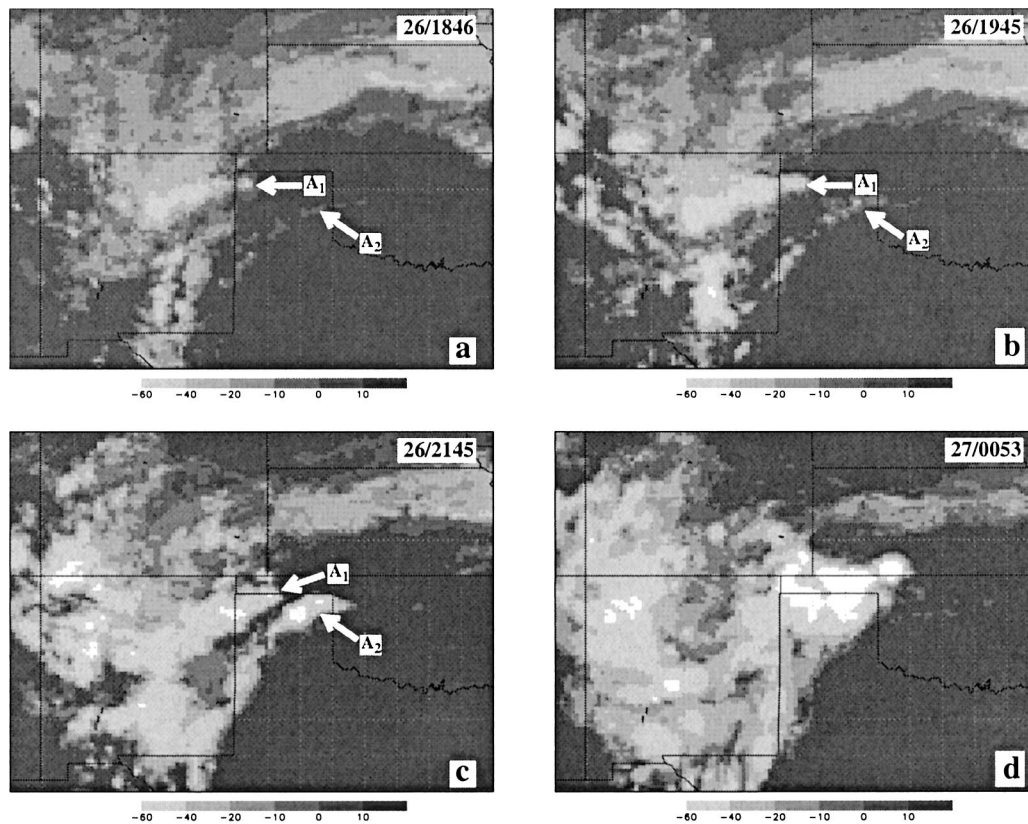


FIG. 1. Satellite imagery from the NCEP Aviation Weather Center (AWS) Infrared Global Geostationary Composite provided by the Global Hydrology Resource Center: (a) 1846 UTC 26 Jul 1998; (b) 1945 UTC 26 Jul 1998; (c) 2145 UTC 26 Jul 1998; and (d) 0053 UTC 27 Jul 1998. White shading represents cloud-top temperature colder than -60°C .

the grids. Convective parameterization was not needed for grid 3 at horizontal grid spacing of 2.5 km, but most mesoscale models generally employ convective parameterization for horizontal grid spacings used in grids 1 and 2 (50 and 12.5 km, respectively). Kain and Fritsch (1998) simulated the 10–11 June 1985 Preliminary Regional Experiment for STORM-Central (PRE-STORM) MCS (Zhang et al. 1989) using the Kain–Fritsch (1990) convective parameterization scheme (K–F CPS) with a nested grid at a horizontal grid spacing of 25 km in the finest grid. Kain and Fritsch (1998) argued that convective parameterization may be necessary even at horizontal grid spacing of 5 km. Gallus and Segal (2001) simulated 20 cases of MCSs with various combinations of different CPSs and model initial conditions using the workstation Eta Model at a horizontal grid spacing of 10 km. Although some cases performed better without convective parameterization, Gallus and Segal found that the model skill scores were higher when they employed a CPS in their simulations. However, for an extensive case study, Warner and Hsu (2000) found that convective parameterization in the coarser grids have negative impacts in the inner grids. They obtained the best result when they excluded convective parameteri-

zation on all the grids and used only explicit microphysics.

Preliminary tests with this case revealed that the model delayed convection in grid 3 by 2 h (as compared to observations) when the K–F CPS was activated in grids 1 and 2. With the K–F CPS activated only in grid 1, RAMS produced results similar to the experiment without the K–F CPS activated in any of the grids. We decided to simulate this case without any convective parameterization in any of the grids for the following reasons: First, using the K–F CPS in grid 2 had negative impact in grid 3. Second, not using the K–F CPS in grid 1 had no large impact in grid 3 (the most important domain). Third, the K–F CPS should be used for horizontal grid spacing of 30 km or less (see MM5 manual online at <http://www.mmm.ucar.edu/mm5/mm5v3/tutorial/teachyourself.html>). So, ideally one should not use the K–F CPS in grid 1. The other option is to use the modified Kuo (1974) CPS in grid 1, but the Kuo CPS is more suited to larger grid sizes. Fourth, our group has obtained very realistic cloud-resolving simulations of MCSs on the finest grid using a similar setup as in this paper without convective parameterization (e.g., Bernardet and Cotton 1998; Nachamkin and Cotton

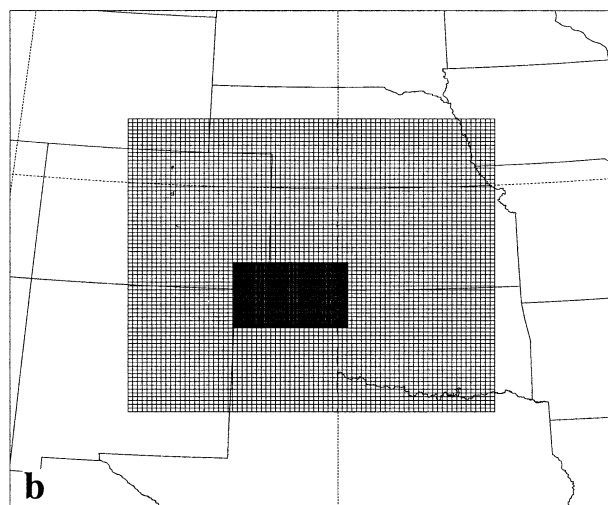
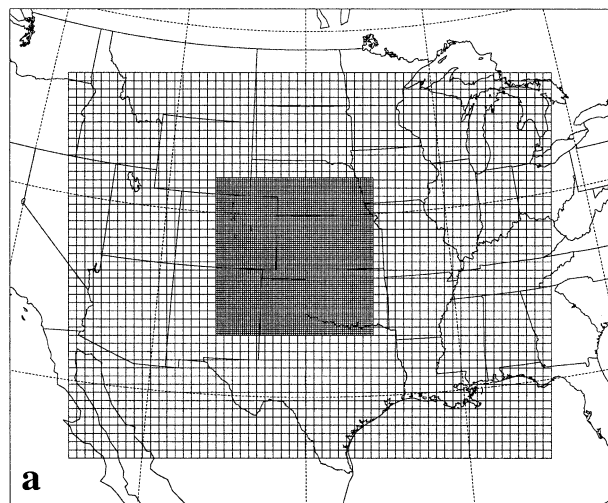


FIG. 2. (a) Nested grid setup in RAMS with grids 1 and 2 and (b) nested grid setup in RAMS with grids 2 and 3.

2000). However, we do not advocate turning off convective parameterization on coarse grids in all situations where cloud-resolving grids are used, especially those designed as forecasting exercises. Nevertheless, in this case, the results were clearly improved by excluding convective parameterization.

a. Model initial conditions

We used the National Centers for Environmental Prediction (NCEP) global analysis to initialize the model atmospheric fields as well as to provide nudging boundary conditions for grid 1's five outermost grid points. The model was initialized by the 1200 UTC 26 July 1998 (26/1200 hereafter) NCEP analysis. Figure 2 shows the nested grid setup. We used two levels of nesting, with horizontal grid spacings of 50, 12.5, and 2.5 km in grids 1, 2, and 3, respectively, and 36 vertical

TABLE 1. Vertical levels (σ_z) used in the simulations (m).

0.0	150.0	300.0	450.0	600.0	750.0
915.0	1096.5	1296.2	1515.8	1757.3	2023.1
2315.4	2636.9	2990.6	3379.7	3807.6	4278.4
4796.2	5365.9	5992.5	6681.7	7439.9	8273.9
9191.3	10 191.3	11 191.3	12 191.3	13 191.3	14 191.3
15 191.3	16 191.3	17 191.3	18 191.3	19 191.3	20 191.3

σ_z levels in each grid (see Table 1), where σ_z is a terrain-following coordinate:

$$\sigma_z = H[(z - z_s)/(H - z_s)], \quad (1)$$

where H is the height of the model top, z_s is the terrain height, and z is the height of the model grid point above sea level (Tripoli and Cotton 1982). We used a grid setup and model physics similar to the current RAMS real-time forecast model in the Cotton research group (<http://rams.atmos.colostate.edu>). We stopped the simulation at 15 model hours after the system of interest moved out of grid 3 (the cloud-resolving grid). We did not use a moving grid to follow the MCS into grid 2 since the moving grid would not retain some of the grid 3 soil moisture. Currently, soil moisture is initialized as horizontally homogeneous in the real-time RAMS forecast model.² So, this study will have practical implications in forecasting MCSs: to determine to what extent heterogeneous soil moisture is important in simulating (or forecasting) MCSs.

At 26/1200, a surface trough extended from Hudson Bay into North Dakota and South Dakota (Fig. 3a). Also, a quasi-stationary front stretched from the Texas/Oklahoma panhandle region, through the Kansas/Oklahoma border, to the southeastern states. South of the quasi-stationary front in the Texas/Oklahoma panhandle, the winds (at the lowest σ_z level) shifted from southerly to westerly because of the influence of the subtropical high over the Gulf of Mexico. Thus, there was low-level convergence along the quasi-stationary front near the MCS genesis region. A surface trough extended from northwestern Oklahoma to the south plains of Texas, and a high pressure was located over central Colorado.

The 850-hPa equivalent potential temperature, θ_e , (Fig. 3b) reveals a wide tongue of high- θ_e air, in a northwest-southeast orientation that stretched from the southeastern states to southern Wyoming, covering most of Colorado and parts of the Texas/Oklahoma panhandle at 26/1200. At this level, weak winds from the north also brought in high- θ_e air to the genesis region. However, the influence of the subtropical high over the Gulf of Mexico did not extend into the Texas/Oklahoma panhandle region.

² In the RAMS real-time model, the soil moisture is specified as 30% saturated in the near-surface levels (0 to 20 cm below surface) and 20% saturated at levels below 20 cm. The soil moisture in one experiment is quite close to the soil moisture initialization in real-time RAMS.

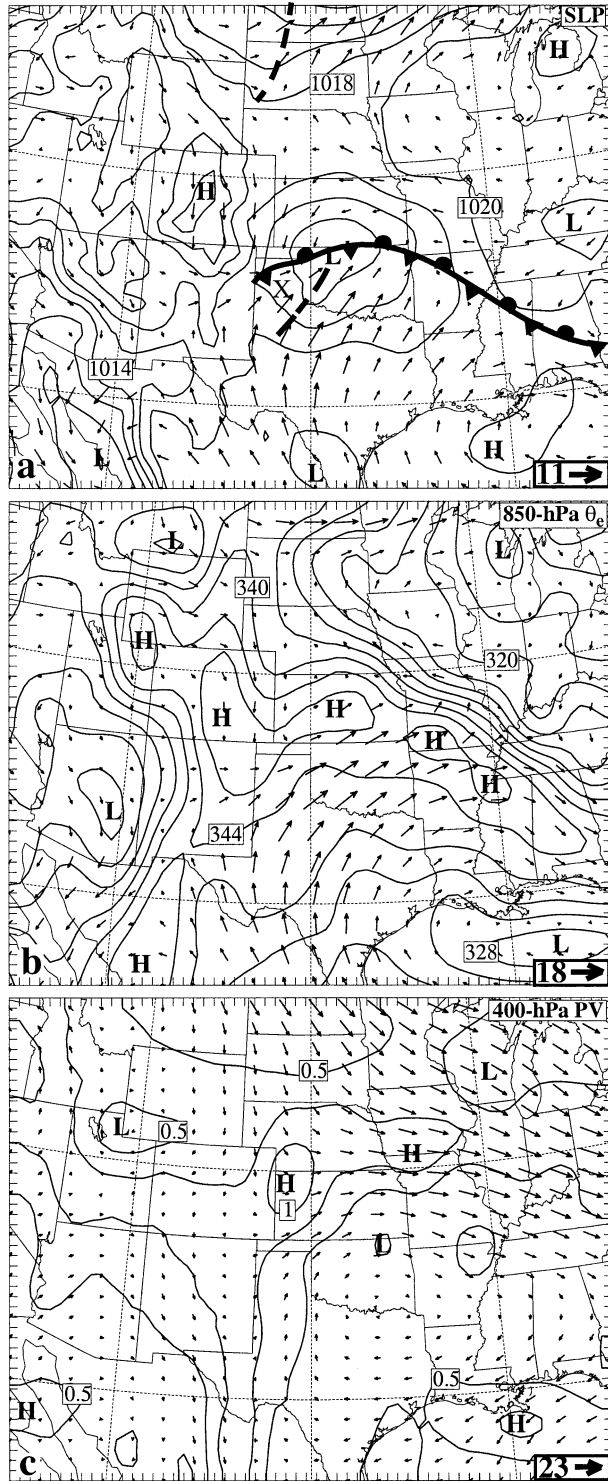


FIG. 3. From the NCEP global analysis interpolated to RAMS grid 1 at 26/1200: (a) sea level pressure (contour intervals of 2 hPa) superposed with wind vectors at the lowest σ_z level; (b) 850-hPa equivalent potential temperature (contour intervals of 4 K) superposed with 850-hPa wind vectors; and (c) 400-hPa potential vorticity (with contour intervals of 0.25 PVU) superposed with 400-hPa wind vectors. Insets represent the scale of the wind vectors in m s^{-1} . In (a) "X" marks the location of Amarillo, TX.

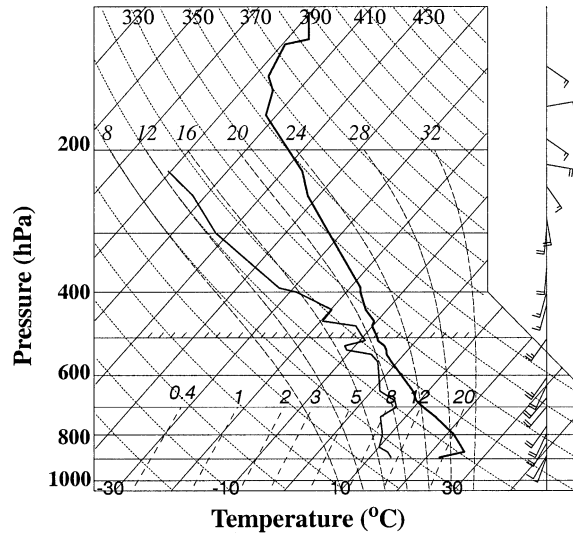


FIG. 4. Skew T -log p diagram for temperature ($^{\circ}\text{C}$), dewpoint temperature ($^{\circ}\text{C}$), and wind (m s^{-1}) on 1200 UTC 26 Jul 1998 at Amarillo, TX ("X" in Fig. 3). A full (half) barb is 5 (2.5) m s^{-1} . Data were obtained at NCAR mass storage.

Figure 3c shows a weak 400-hPa potential vorticity (PV) band to the north of the Texas/Oklahoma panhandle that was associated with a dissipating MCS at the model initial time. Winds at this level were weak as well, and there was no upper-level feature upstream of the genesis region at this time.³ A sounding (Fig. 4) closest to the genesis region (Amarillo, Texas; Fig. 3a) shows weak winds throughout the entire column, and little directional or speed shear from the surface to 500 hPa. From the surface to 400 hPa, the wind was from the southwest, then backed to southerly between 400 and 300 hPa. Above 300 hPa, the wind backed to easterly. The sounding only had a value of 670 J kg^{-1} in convective available potential energy (CAPE) because of the dry soil condition (discussed in the next subsection). There was a shallow inversion layer at the surface (about 25 hPa deep). At this time, the atmosphere was relatively dry (moist) from the surface to 700 hPa (from 700 to 475 hPa).

b. Soil moisture and sensitivity experiments

The soil moisture was exceptionally low in the Texas/Oklahoma panhandle region for the summer of 1998

³ The 400-hPa PV from the Eta Data Assimilation System (EDAS) analysis (<http://www.emc.ncep.noaa.gov>) reveals more structure because of its finer resolution, available at 40-km grid spacing (figure not shown). At 400 hPa, a PV maximum of 1.5 PVU ($1 \text{ PVU} = 10^{-6} \text{ m}^2 \text{ K kg}^{-1}$) was located upstream of the Texas/Oklahoma panhandle. It is possible that this PV maximum played a role in the development of the MCS. However, we did not use this finer-resolution dataset to initialize RAMS. Simulations run with EDAS initialization produced disorganized convection and failed to produce a quasi-circular cloud shield because of the weaker southeast-northwest-oriented θ_e tongue (covering the genesis region) in the EDAS initialization (Fig. 3b).

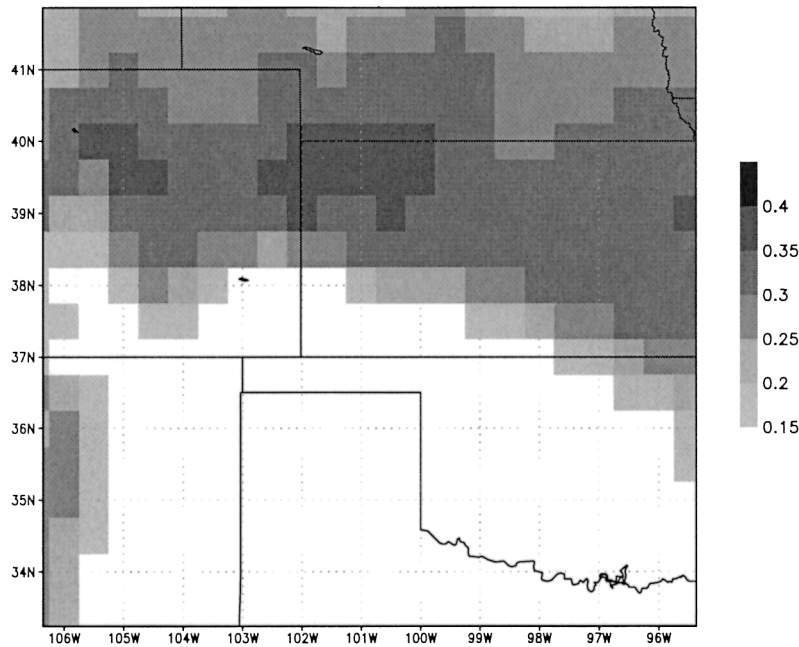


FIG. 5. The 0–10-cm volumetric soil moisture ($\text{m}^3 \text{m}^{-3}$) from EDAS.

because of the record low rainfall between April and June 1998. This extremely dry soil condition reached levels comparable to or worse than the 1930s Dust Bowl. The severe drought in the Texas/Oklahoma panhandle did not end until early fall of 1998 (Basara et al. 1999; Bell et al. 1999; Hong and Kalnay 2002). Figure 5 shows the 0–10-cm volumetric soil moisture (see the appendix for the meaning of volumetric soil moisture) from the EDAS⁴ on 1200 UTC 26 July 1998. The volumetric soil moisture content was less than $0.15 \text{ m}^3 \text{ m}^{-3}$ in the Texas/Oklahoma panhandle. Of note, rainfall from several MCSs during July 1998, including the one in this paper, provided some relief to the drought in the Texas/Oklahoma panhandle region.

In our simulations, soil moisture for grid 3 was inferred from the Global Energy and Water Cycle Experiment (GEWEX) Continental-Scale International Project (GCIP) (Information online at <http://www.joss.ucar.edu>) precipitation archive by using the antecedent precipitation index (API; Chang and Wetzel 1991). This GCIP precipitation dataset has a grid spacing of 4 km and covers a large portion of the continental United States. The algorithm to convert the API values to volumetric soil moisture is presented in the appendix. Note that the soil moisture heterogeneities in grid 3 were exaggerated (see the appendix). This is not unlike previous experiments in climate models where “superan-

omalies” in SST were introduced to gain better understanding in air–sea interaction (Dirmeyer 1995). This method is preferable to placing “checkerboard” soil moisture patches.

We did not use the API method to initialize soil moisture in grid 1 because of the limited area of the GCIP precipitation data (it does not cover Mexico in grid 1). Instead, we used the EDAS soil moisture (40-km grid spacing) to initialize grid 1. Furthermore, we chose the soil moisture in grid 2 to come from the same source as grid 1. Of note, we used the Rapid Update Cycle (RUC; information available online at <http://ruc.fsl.noaa.gov>) soil moisture (40-km grid spacing) in grids 1 and 2 and found no significant difference in the results of grid 3. In addition, we have used homogeneous soil moisture initialization in grids 1 and 2 and found no significant impact in grid 3. The homogeneous soil moisture values were obtained by horizontally averaging the soil moisture in grids 1 and 2 originally initialized by EDAS soil moisture. Thus, we are confident that using different soil moisture datasets in different grids did not have significant impact on the cloud-resolving grid containing the MCS genesis domain.

Given the inexact nature of the API method, it is difficult to estimate the deep-layer soil moisture. So, for simplicity, we assumed the soil moisture to be constant with depth for grid 3. For the short-term simulations in this study, the near-surface soil moisture in grid 3 is more important than the deep-layer soil moisture where sparse vegetation is dominant.

To alter the resolution of the grid 3 soil moisture, we applied the Barnes (1964) objective analysis to smooth the soil moisture with a response amplitude (A) of 0.5

⁴ The July 1998 EDAS soil moisture was continuously cycled without soil moisture nudging (e.g., to some climatology). In addition, the July 1998 EDAS soil moisture was the sole product of model physics and internal EDAS surface forcing (e.g., precipitation and surface radiation). More information on the soil moisture cycling in EDAS can be obtained from Ek et al. (2003).

TABLE 2. List of numerical experiments.

Expt	Description
API	Soil moisture in grid 3 derived from API method.
API20	Grid 3 soil moisture in expt API smoothed by Barnes objective analysis with a response amplitude of 0.5 and a cutoff wavelength of 20 km.
API40	Same as expt API20 but with a cutoff wavelength of 40 km.
API80	Same as expt API20 but with a cutoff wavelength of 80 km.
APIHALF	Grid 3 soil moisture in expt API divided by 2.
APIMOVES2	Soil moisture anomaly, S_2 , in grid 3 from expt API displaced southwestward.
HOM31	Homogeneous soil moisture in grid 3 at 31% saturation, a value obtained by horizontally averaging the grid 3 soil moisture in expt API.
HOM50	Homogeneous soil moisture in grid 3 at 50% saturation.

and a cutoff wavelength (λ_{cut}) of 20 (expt API20), 40 (expt API40), and 80 (expt API80) km. To alter the amplitude of the soil moisture field, we reduced the soil moisture in expt API by a factor of 2 (expt APIHALF). A soil moisture anomaly in the eastern Texas panhandle in expt API was displaced southwestward in grid 3 (expt APIMOVES2). An experiment (HOM31) was also performed with homogeneous soil moisture initialization in grid 3 (at 31% saturation) by using the horizontally averaged grid 3 soil moisture in expt API. We also performed another homogeneous soil moisture experiment at 50% saturation in grid 3 (expt HOM50⁵). A summary of the experiments is listed in Table 2. An additional reason for using the EDAS soil moisture to initialize grid 2 is that we did not want grid 2 (unsmoothed) soil moisture to have a higher resolution than that of grid 3 in some of the sensitivity experiments (with smoothed SMI). We only wanted to vary the soil moisture of the cloud-resolving grid (grid 3) while keeping everything else the same.

The initial soil moisture fields for grid 3 for the various sensitivity experiments are displayed in Fig. 6. Two large soil moisture anomalies can be identified in grid 3, one in the northwest corner (S_1) and one near the center of the domain (S_2). Because of the proximity of some soil moisture anomalies to one another, we refer to some of them as a single unit for ease of reference. With increasing λ_{cut} , Barnes objective analysis eliminated finer-scale features in larger soil moisture anomalies (S_1 and S_2) and also reduced the horizontal extent of the smaller soil moisture anomalies (S_3 and S_4). In all the experiments, 11 soil levels were used (Table 3).

c. Normalized Difference Vegetation Index

We used the Normalized Difference Vegetation Index (NDVI) at 1-km grid spacing, provided by the Earth Resources Observation Systems (EROS) Data Center, to compute the leaf area index (LAI) for LEAF-2. We

do so by first deriving the fractional area of green vegetation from the NDVI and then we use this fractional area to derive the LAI.

The NDVI is defined as (Carlson and Ripley 1997)

$$\text{NDVI} = \frac{(a_{\text{nir}} - a_{\text{vis}})}{(a_{\text{nir}} + a_{\text{vis}})}, \quad (2)$$

where a_{nir} and a_{vis} are the surface reflectance averaged over the near-infrared and visible parts of the spectrum, respectively. The NDVI varies between -1 and 1 . Healthy vegetation has a high albedo in the near-infrared region; thus, a positive NDVI indicates a state of healthy vegetation. We used a variation of the formula from Chang and Wetzel (1991) to compute the “green” vegetation fractional area (v_{frac}):

$$v_{\text{frac}} = \frac{(\text{NDVI} - \text{NDVI}_{\text{min}})}{(\text{NDVI}_{\text{max}} - \text{NDVI}_{\text{min}})}, \quad (3)$$

where NDVI_{min} and NDVI_{max} correspond to the minimum and maximum NDVI, respectively. We chose the minimum and maximum NDVI from a 10-yr record (1991–2000) for each 1-km² pixel. This pixel-specific method of finding the maximum/minimum NDVI differs from the method of Sellers et al. (1994). The maximum/minimum NDVI is biome-specific in the Sellers et al. (1994) method, and the maximum (minimum) is chosen from the 98th (2nd) percentile of a $1^\circ \times 1^\circ$ global annual dataset. The advantage of the algorithm in this paper (J. Eastman 2001, personal communication) is that the maximum (or minimum) NDVI is pixel or geographically specific rather than single valued. However, there is a problem with this method (to be explained in the next paragraph).

Next, we performed a weighted areal average of the “green” vegetation fraction for the area occupied by the RAMS grid element. Using a similar formula in Sellers et al. (1994), the LAI for the i th patch within the RAMS grid area is

$$\text{LAI}_i = (\text{LAI}_{\text{max},i})(v_{\text{frac}}), \quad (4)$$

where $\text{LAI}_{\text{max},i}$ corresponds to the maximum LAI of the particular biome-matching patch i . We used the maximum LAI values from LEAF-2 (Table 4). The vegetation biome class dataset in RAMS has a grid spacing

⁵ We should point out that the soil is still considered dry at 50% saturation or $0.21 \text{ m}^3 \text{ m}^{-3}$ in volumetric soil moisture. Luo et al. (2003) found the lowest mean volumetric soil moisture in the 0–40-cm layer during the May–July 1998 drought in Oklahoma to be $0.22 \text{ m}^3 \text{ m}^{-3}$.

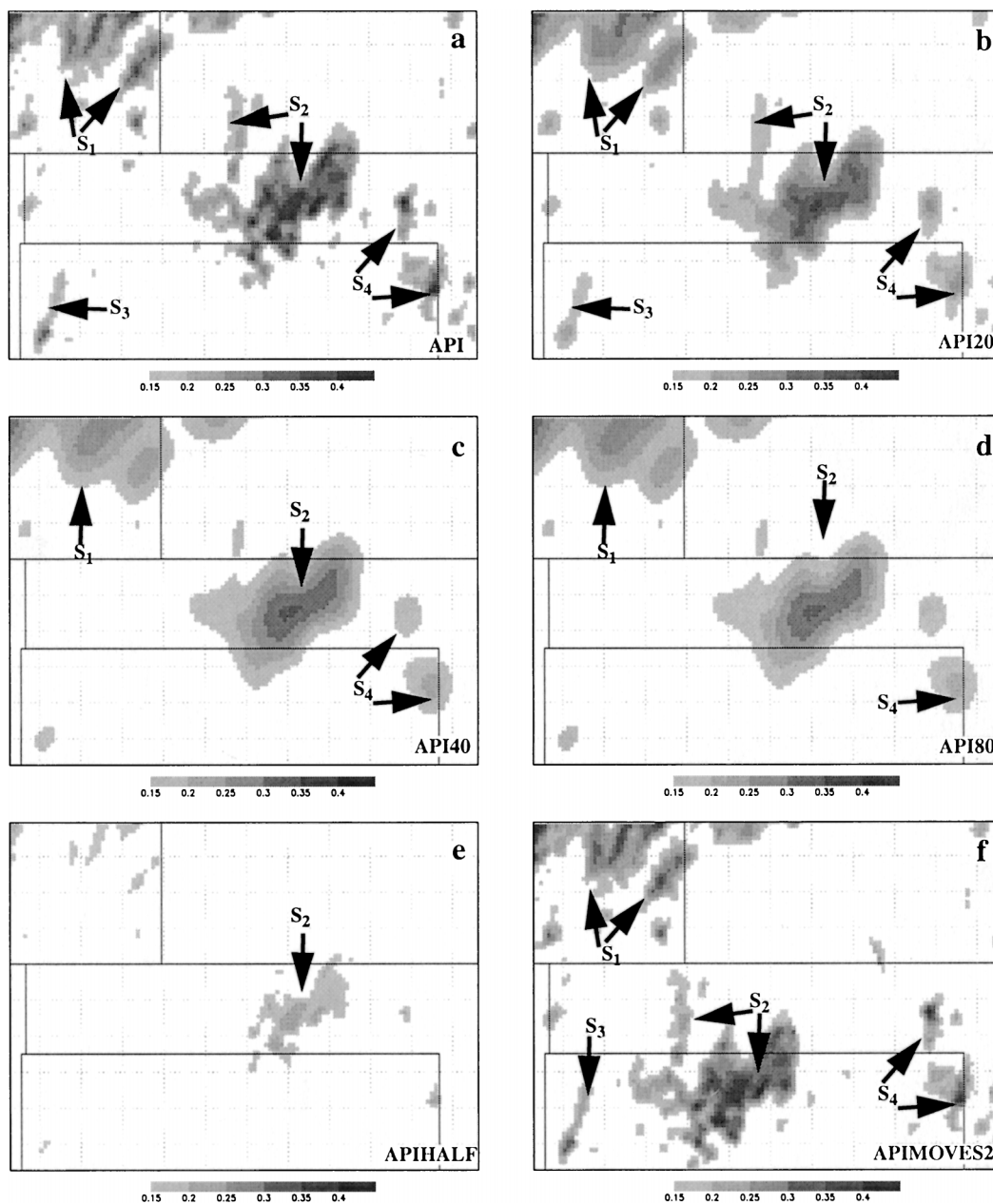


FIG. 6. Initial volumetric soil moisture ($m^3 m^{-3}$) in grid 3 for expts (a) API, (b) API20, (c) API40, (d) API80, (e) APIHALF, and (f) APIMOVES2.

of 30 s. Note that in the default computation of LAI in RAMS, the LAI for each patch is matched according to the biome type of that particular patch, with a time-dependent factor to account for the season. A comparison of the default LAI and the NDVI-derived LAI shows that the default LAI is rather homogeneous with

a value of 6 (a bit too high for the region) throughout most of the domain. On the other hand, the NDVI-derived LAI, being more heterogeneous, varies from 1 to 5, with an average value of about 3 (Fig. 7). Thus, using the NDVI data allows for more spatial variability and realism in defining the LAI. However, as mentioned in the previous paragraph, there is a problem with the NDVI to LAI conversion. The LAI values may be a bit too high in some situations. For example, sparse vegetation can reach a green vegetation fraction close to unity if the NDVI reaches its maximum value for a

TABLE 3. Soil levels (below ground) used in the simulations (m).

1.02	0.92	0.82	0.72	0.62	0.52
0.42	0.32	0.22	0.12	0.02	

TABLE 4. Maximum LAI of various biomes in RAMS.

Biome	Max LAI
Crop/mixed farming	6.0
Short-grass	2.0
Evergreen needleleaf tree	6.0
Deciduous needleleaf tree	6.0
Deciduous broadleaf tree	6.0
Evergreen broadleaf tree	6.0
Tallgrass	3.0
Desert	0.0
Tundra	3.0
Irrigated crop	3.0
Semidesert	4.0
Bog or marsh	3.0
Evergreen shrub	5.0
Deciduous shrub	5.0
Mixed woodland	6.0

particular pixel. This caused problems in a few areas (albeit small) in grid 3 where the LAI exceeded 5. However, only a small fraction of the pixels was affected.

4. Model results

a. Grid 1

We compare the grid 1 fields with those in the NCEP analysis in order to evaluate how well RAMS reproduced the large-scale flow. First, we examine the fields from the NCEP analysis at 27/0000 (Fig. 8). By this time, the western end of the quasi-stationary front has moved southeastward, away from the Texas/Oklahoma panhandle region. The outflow boundary (identified by the National Weather Service and labeled in Fig. 8a) from convection in New Mexico and the MCS in the

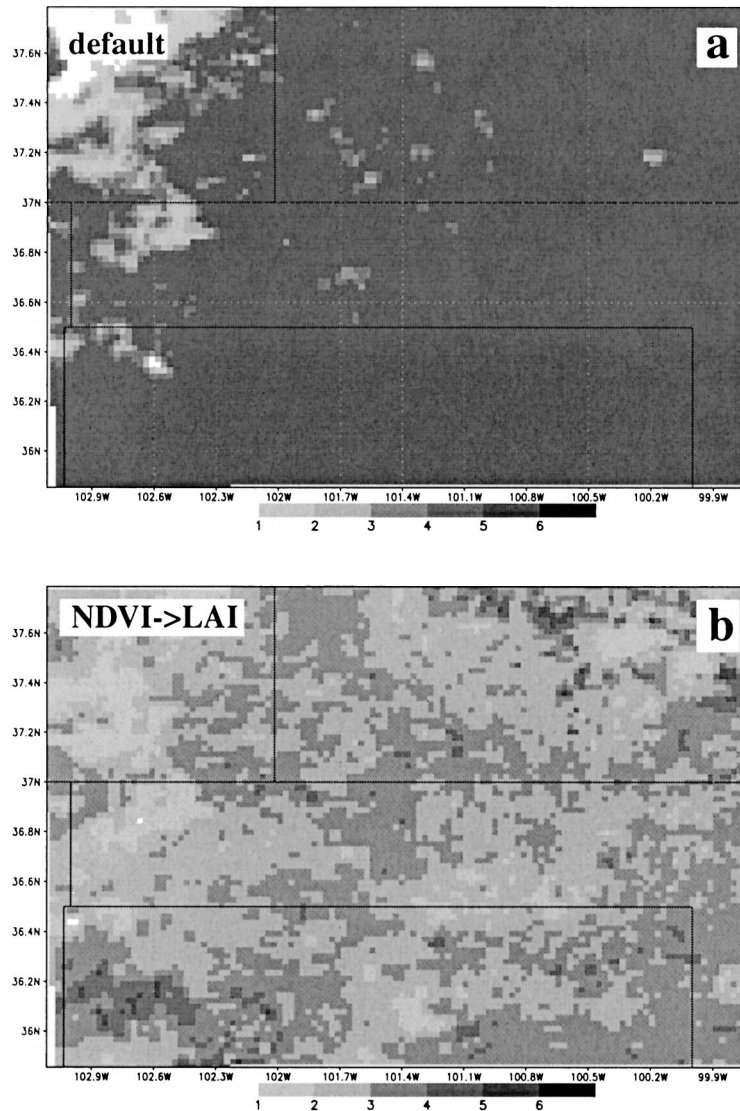


FIG. 7. (a) Default leaf area index in RAMS grid 3 and (b) NDVI-derived leaf area index in RAMS grid 3.

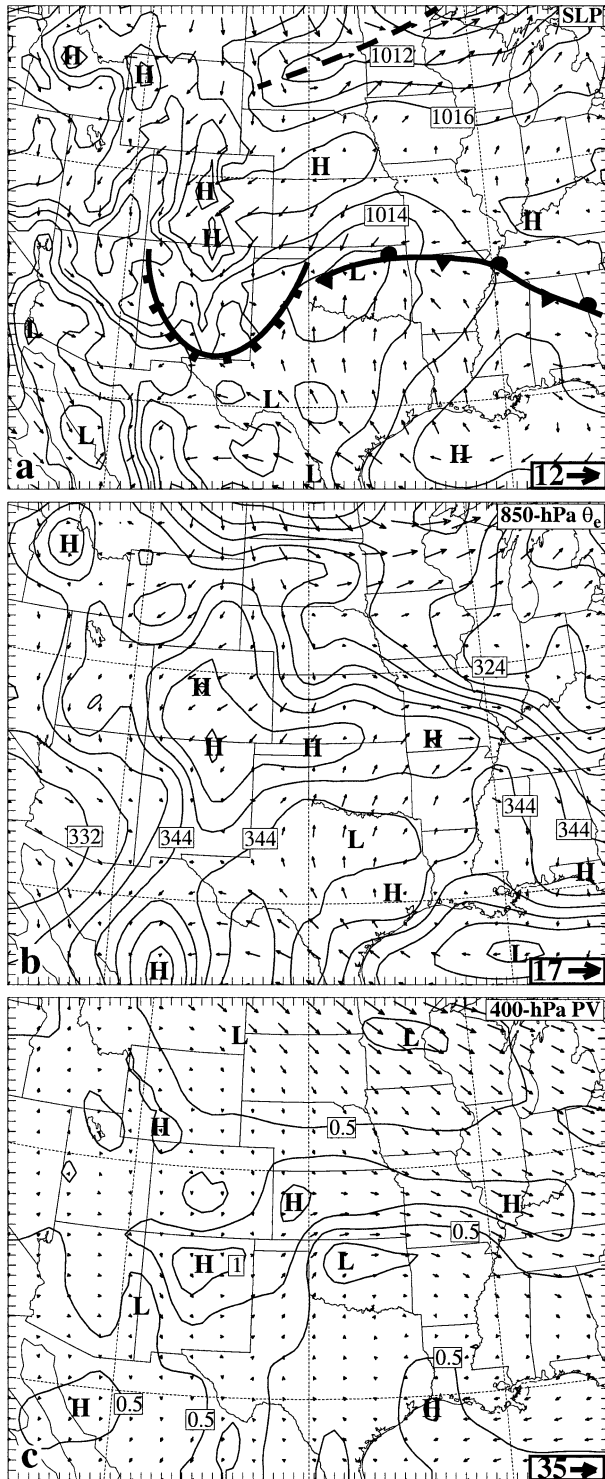


FIG. 8. As in Fig. 3, but for 27/0000. The solid curve with square symbols in (a) represents outflow boundaries.

Texas/Oklahoma panhandle distorted the quasi-stationary front in the Texas/Oklahoma panhandle. There was a region of surface wind convergence in the Texas/Oklahoma panhandle region due to the deceleration of the wind from the north. The 850-hPa high- θ_e tongue that covered the Texas/Oklahoma panhandle region has increased by 4 K at this time. The 400-hPa PV map shows a weak PV maximum embedded within a PV band, upstream of the panhandle. This PV maximum was of diabatic origin (associated with convection over New Mexico). As with 12 h earlier, the winds at 400 hPa were still weak.

Next, we examine the grid 1 results from expt API (Fig. 9) at 27/0000. Other experiments produced similar results for grid 1 and will not be shown for the sake of economizing space. The sea level pressure in expt API compares reasonably well with that of the NCEP analysis, except that the simulated surface low over Oklahoma was a bit too far to the west and 2 hPa too low. The outflow boundary (identified in grid 2) was not as accurately predicted because of the model's inability to capture the convection in New Mexico. The 850-hPa θ_e compares reasonably well with NCEP analysis albeit with a few discrepancies. The simulated θ_e maxima did not extend as far into Colorado. In expt API, the 850-hPa southwesterlies (associated with the subtropical high over the Gulf of Mexico) over eastern Oklahoma was a bit stronger than those in the NCEP analysis. Similar to observations, the simulated PV band at 400 hPa in expt API stretched northeastward from New Mexico into the Texas/Oklahoma panhandle and Kansas. However, the maxima in the simulated PV band (due to diabatic heating) were too large over the Texas/Oklahoma panhandle. Nevertheless, RAMS reproduced the large-scale features fairly well at this time.

b. Grid 2

An examination of expt API's grid 2 cloud-top temperature (defined as the temperature of the total condensate mixing ratio $>0.1 \text{ g kg}^{-1}$ at the highest elevation of the atmospheric column) shows convective activity at the Texas/Oklahoma panhandle at 26/2200 (Fig. 10a). However, the shape of the simulated cloud top was somewhat different than in the satellite imagery (Fig. 1c). In addition, the simulated convective activity was a bit too far north than in the satellite imagery. Furthermore, we observed two distinct convective regions in the eastern and western panhandle that were not simulated in expt API (Figs. 1c and 10a). Nevertheless, by 27/0100 in expt API, a quasi-circular cloud shield (Fig. 10b) similar to observations (Fig. 1d) developed over the Texas/Oklahoma panhandle region, but the simulated cloud shield extended too far into Kansas. Although there was some deep convection over New Mexico in expt API by 27/0100, the model did not capture the widespread convection over New Mexico. This could be explained by the fact that there was no cloud-

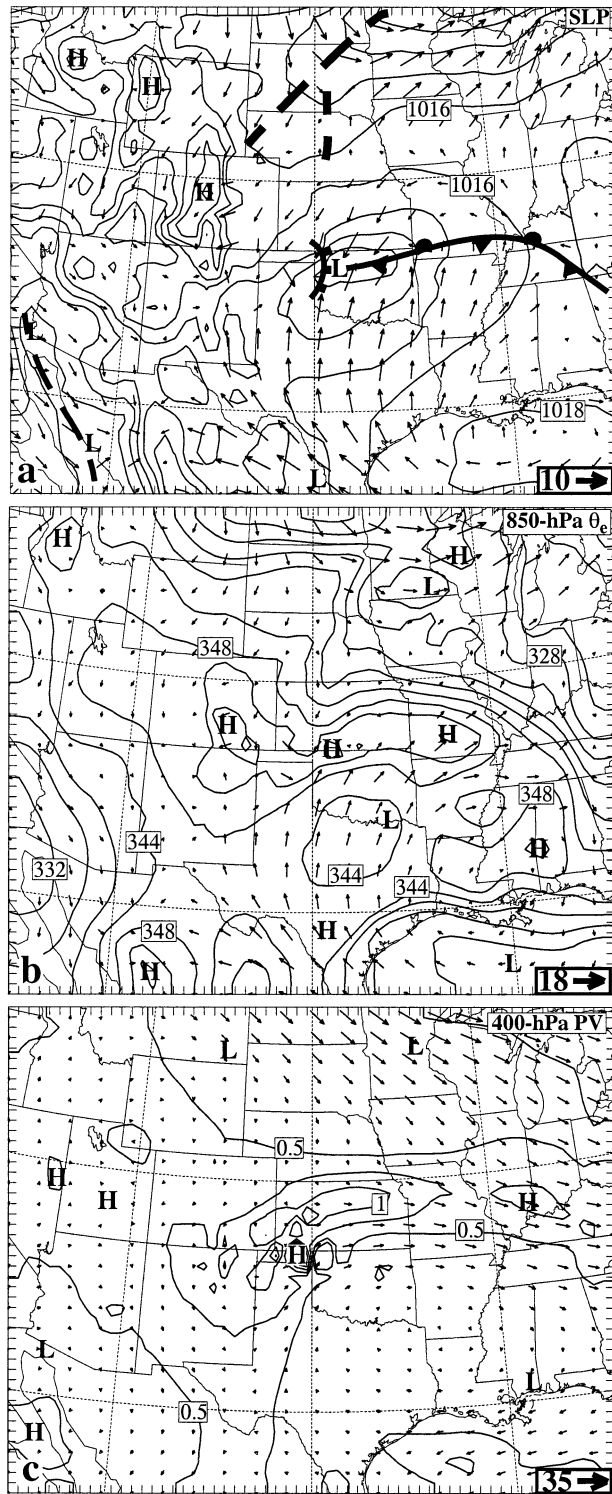


FIG. 9. As in Fig. 3, but for expt API at 27/0000.

resolving grid placed over New Mexico. Thus, convection was not well resolved there. Still, RAMS managed to produce an MCS in the area close to the one observed with a similar shape at the right time. Other sensitivity

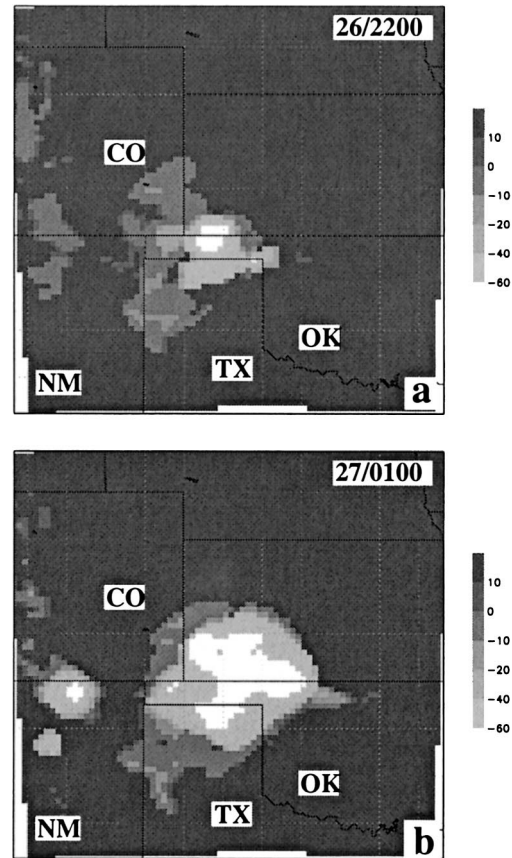


FIG. 10. Expt API cloud-top temperature for grid 2 at (a) 26/2200 and (b) 27/0100. CO, NM, TX, and OK stand for Colorado, New Mexico, Texas, and Oklahoma, respectively. White shading represents cloud-top temperature colder than -60°C .

experiments (except for expt HOM50) produced similar results, so again for the sake of brevity, they will not be shown.

c. Pregenesis phase: Grid 3

As expected, the surface latent heat flux (SLHF) pattern corresponds quite well to the soil moisture distribution in grid 3 (figure not shown). Peak SLHFs in S_2 for expts API, API20, API40, and API80 were 455, 450, 430, and 377 W m^{-2} , respectively. Values of SLHF from expt HOM31 were generally 100 W m^{-2} or less. Because the wet soil moisture anomalies contributed to enhanced moisture fluxes in expts API, API20, API40, and API80, the Bowen ratio [surface sensible heat flux (SSHf) divided by SLHF] was generally less than 0.5 over the wet soil moisture anomalies (not shown). In very wet (dry) soil areas, the Bowen ratio was less than 0.25 (greater than 2).

Figure 11 shows the dewpoint temperature at the lowest σ_z level above ground at 26/1800 for expt API. Results from other experiments are not shown to economize space. The influence of the soil moisture anoma-

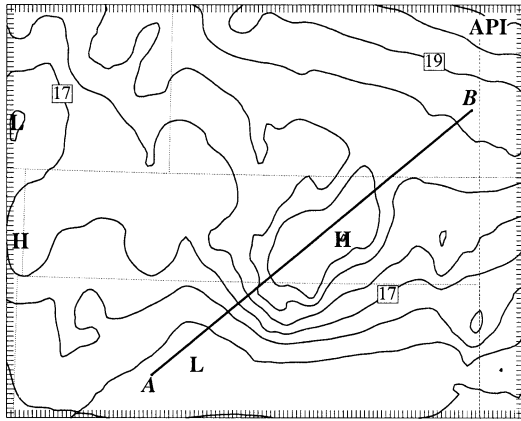


FIG. 11. RAMS grid 3 dewpoint temperature at the lowest σ_z level above ground (at contour intervals of 0.5°C) at 26/1800 for expt API.

lies, especially S_2 , raised the dewpoint at this level by almost 2°C as compared to expt HOM31 (not shown). Smaller soil moisture anomalies such as S_3 and S_4 had less noticeable effects on the dewpoint at this level, and their effects were even smaller with increased smoothing of the SMI. The effects of S_1 were not as noticeable as S_2 because of the smaller size of S_1 and its proximity to the lateral boundaries. However, S_1 did raise the dewpoint by about 1°C . Expt HOM50 had the highest dewpoint among all the other experiments because of the high SLHF (not shown).

To quantify the dynamical effect of the soil moisture anomalies at 26/1800, using expt HOM31 as a baseline, we took the difference fields of the sea level pressure, the horizontal wind vector, and the vertical velocity at the lowest σ_z level (Fig. 12). First, we discuss the results of expts API, API20, API40, and API80. The cooling effect of the soil moisture anomaly S_2 created a mesohigh on the order of 0.5 hPa at sea level as well as a divergent flow perturbation (on the order of 4 m s^{-1}) at the lowest σ_z level. It is interesting to note that the divergent flow perturbation maximum (associated with S_2) increased slightly from 3.6 to 4.1 (4.4 m s^{-1}) when the soil moisture was smoothed with λ_{cut} of 20 (40) km. This can be attributed to the internal circulations generated by the finescale soil moisture features opposing the mesoscale circulation induced by the larger-scale soil moisture feature in S_2 as a whole. However, when the smoothing reached a cutoff wavelength of 80 km, the divergent flow perturbation maximum decreased to 4.1 m s^{-1} . At this point, with λ_{cut} at 80 km, most of the finescale features have been eliminated, and the large-scale structure of the soil moisture has been smoothed too much, leading to weaker NCMCs. With regard to S_1 for the four aforementioned experiments, the associated mesohigh (on the order of 0.25 hPa) and the divergent flow perturbation were somewhat weaker and smaller in coverage than those of S_2 . However, the smoothing of the soil moisture seemed to expand the

coverage of the mesohigh associated with S_1 . The effects of S_3 were weak because of its small size and shielding from low-level cloud (not shown); S_3 almost disappeared when the smoothing reached a cutoff wavelength of 40 km. Although the mesohigh generated by S_4 was less than 0.25 hPa, the NCMC from S_4 generated small regions of anomalous vertical motion (on the order of $2\text{--}4\text{ cm s}^{-1}$). However, the influence of S_4 diminished (disappeared) when the smoothing reached a cutoff wavelength of 40 (80) km.

In expt APIHALF (Fig. 12e), because of the reduced SLHF (in terms of area and magnitude), the mesohigh generated by S_2 was less than 0.25 hPa, and the divergent wind perturbation associated with S_2 was less than 2 m s^{-1} . The effects of other soil moisture anomalies in expt APIHALF are harder to discern. As expected, with S_2 displaced in expt APIMOVES2, the anomalous mesohigh associated with S_2 shifted southwestward. Because of the higher values of SLHF (thus a cooler surface) in expt HOM50, the sea level pressure was higher in expt HOM50 throughout most of its domain when compared to expt HOM31 (Figs. 12f,g). In general, the anomalous vertical motion generated by the soil moisture anomalies reached several centimeters per second at this time.

To determine the depth of the mesohigh generated by S_2 , we took a cross section of the horizontal temperature deviation through S_2 at 26/1800 (Fig. 13). To obtain the temperature deviation, we subtracted the temperature field from the average temperature at each constant height level. Since the experiments with heterogeneous SMI had similar results, we will only show results from expt API. The depth of the cold pool associated with the mesohigh generated by S_2 was about 1.5 km, and its temperature deviation was on the order of 1 K. This cold pool suppressed convection because of its enhanced stability. However, acting as a focusing mechanism for convection to develop, the leading edge of this cold pool resembled a sea breeze front, providing anomalous vertical motion around the periphery of S_2 (Fig. 12).

d. Genesis phase: Grid 3

We examine the convective activity in the cloud-resolving grid using the instantaneous precipitation rate. With the exception of expts APIMOVES2 and HOM50, all the experiments had very similar results at 26/1915 (Fig. 14). There were two weak precipitation features in the western Oklahoma panhandle: C_1 and C_2 , which originally formed in the western Texas panhandle area at 26/1500 as very weak precipitation features ($\sim 1\text{ mm h}^{-1}$) and slowly moved northward. There was also a strong convective cell, C_3 , in the middle of the Texas panhandle that formed in response to the build up of CAPE and low-level convergence along the quasi-stationary front. Compared to the satellite imagery at 26/1945 (Fig. 1b), the model placed the precipitation a bit too far north and east of the Texas panhandle at this

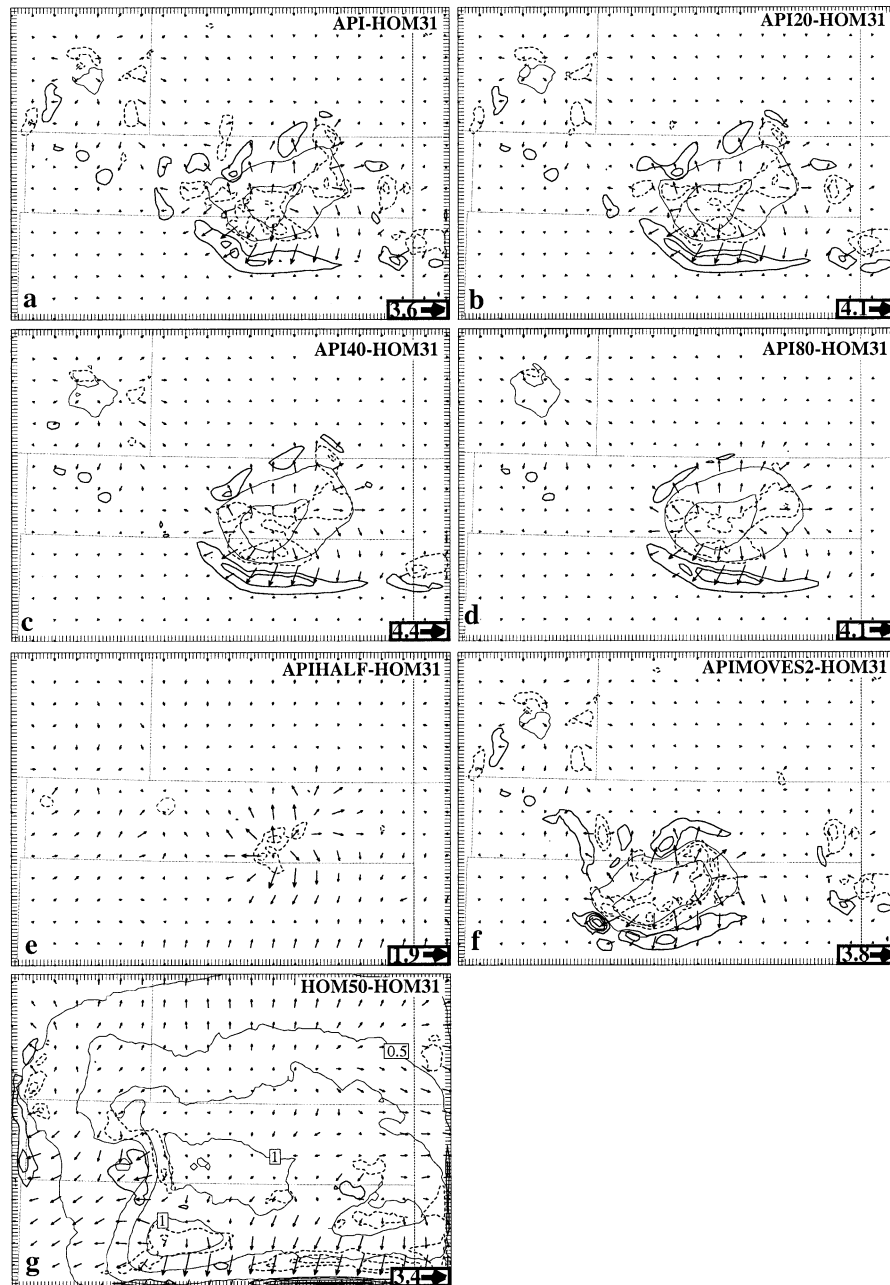


FIG. 12. RAMS grid 3 vertical velocity difference at the lowest σ_z level above ground (thick contours, every 2 cm s^{-1}) and sea level pressure difference (light contours, every 0.25 hPa) superposed with the difference in horizontal wind vectors at the lowest σ_z level above ground at 26/1800 for expts (a) API-HOM31, (b) API20-HOM31, (c) API40-HOM31, (d) API80-HOM31, (e) APIHALF-HOM31, (f) APIMOVES2-HOM31, and (g) HOM50-HOM31. Solid (dashed) contours represent positive (negative) values, and zero contour is suppressed. Insets represent the scale of the wind vectors in m s^{-1} .

time. Of note, at this time, the convection along the surface trough in the Texas panhandle region (A_2 in Fig. 1b) was not captured by the model (see Fig. 3a). There are several possibilities for this. First, grid 3 (Fig. 2b) was not sufficiently large to cover the area where the convective line A_2 initiated (Fig. 1b). Second, grid 2

did not capture A_2 . Although grid 2 failed in this case to capture A_2 , our experience with RAMS in real time suggests that in some events, a horizontal grid spacing of 12 km is sufficient to resolve the gross features of convective events. Those cases are probably more strongly forced than the case in this study in which a

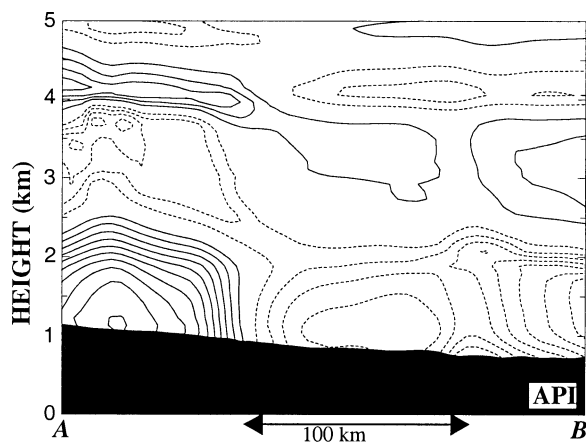


FIG. 13. (a) Vertical cross section of horizontal temperature deviation (at contour intervals of 0.25 K) taken through lines in Fig. 11 for expts (a) API and (b) API80 at 26/1800. Zero contour is suppressed, and solid (dashed) contours represent positive (negative) values.

horizontal grid spacing of 12.5 km in grid 2 did not have sufficient resolution to resolve A_2 . If grid 2 had been able to capture the gross features of A_2 , grid 3 might have been able to simulate A_2 when it enters its domain. Third, the upper-level PV maximum (upstream from the genesis region) missing in the model initialization from the NCEP analysis (footnote 3) might have caused the model not to initiate A_2 . Still, the timing of the model convection was reasonably good. Precipitation feature C_2 was rather weak and would dissipate shortly after this time. Expt HOM31 (Fig. 14g) generated results similar to experiments with heterogeneous SMI (except for expt APIMOVES2). In expt APIMOVES2, the cooling effect of S_2 suppressed the initiation of convective cell C_3 at this time. In a similar manner, convection was suppressed in expt HOM50 at this time. Next, we examine how the soil moisture heterogeneities affected the evolution of convection.

At 26/2145, convection was becoming more organized for most of the experiments (Fig. 15). First, we discuss the results in expts API, API20, API40, and API80. Qualitatively, expts API, API20, API40, and API80 had similar results. Precipitation feature C_1 precipitated more heavily with the smoothing of the SMI because of the enhanced NCMC associated with S_1 . The NCMC generated by S_2 provided a focusing mechanism for convective features C_3 and C_4 to develop along the periphery of S_2 (Figs. 15a–d) because of the enhanced vertical motion there (Fig. 12). Convective feature C_4 was generated 1 h earlier because of the remnant of the weak outflow boundary from C_2 (Fig. 14) interacting with the NCMC generated by the soil moisture anomaly S_2 . The outflow of C_4 generated C_7 ahead of it except in expt API40 in which C_7 emerged 30 min later. Convective cell C_6 was created when the NCMCs generated by the northern and southern ends of S_4 collided. The outflow from C_3 also assisted in the initiation of C_6 . As

S_4 was smoothed, leading to a reduction of its associated NCMC, C_6 was reduced in intensity.

Next, we discuss the results for the other experiments at 26/2145 (Figs. 15e–h). In expt APIHALF, with S_2 at half its magnitude as in expt API, the NCMC associated with S_2 was weaker. As a result, the enhanced vertical motion around S_2 was much smaller (Fig. 12). Thus, C_3 and C_4 did not track around S_2 as much, but moved closer to the interior of the much drier S_2 . Convective cell C_6 did not form because the NCMC associated with S_4 was negligible. Expt APIMOVES2 produced results qualitatively similar to expt API, but C_3 did not appear. Convective cell C_6 in expt APIMOVES2 was also weaker than that of expt API because of the absence of the outflow boundary associated with C_3 interacting with the NCMC of S_4 . In expt HOM31, because of lack of NCMC (from S_2) interacting with C_3 , C_3 could cross the Oklahoma panhandle more easily. Convective cell C_6 was expectedly absent in expt HOM31 because of the lack of soil moisture anomaly S_4 . Convection was finally initiated in expt HOM50 at this time, including the appearance of a multicellular system in the middle of the Texas/Oklahoma border. The delay in convection in expt HOM50 was due to a cooler surface associated with a higher SLHF, making convection harder to initiate.

By 26/2300, in all the experiments (except expt HOM50), the outflow boundaries of various cells have merged into a convective line with a southeast–northwest orientation, just north of the Oklahoma panhandle (Fig. 16). The convective lines in expts API, API20, API40, and API80 were very similar to each other. Because of the weaker NCMC from S_2 interacting with the convective line in expt APIHALF, the convective line advanced farther into the eastern edge of the domain. The convective line in expt APIMOVES2 was a bit shorter compared to other experiments because of the absence of C_3 (Figs. 14 and 15). Qualitatively, the convective line in expt HOM31 was similar to that in other experiments, but expt HOM50 failed to develop a convective line. Also, convection was not well organized in expt HOM50.

The time series of grid 3 domain-averaged SLHF show expt HOM50 (APIHALF) to have the highest (lowest) SLHF (Fig. 17a). This is not surprising since the stomatal response function (a parameter controlling evapotranspiration; Avissar and Pielke 1991; Golaz et al. 2001) was almost unity (zero) for most of the domain in expt HOM50 (APIHALF), allowing the most (the least) transpiration. All the other experiments fell somewhere between the two extremes. Expt HOM31 had slightly lower SLHF than expts API, API20, API40, API80, and APIMOVES2 between 26/1600 to 26/2100. The SSHF time series (Fig. 17b) reveal a completely opposite trend as compared to the latent heat time series because of the influence of soil moisture in partitioning the SSHF and SLHF. The highest (lowest) sensible heat flux was from expt APIHALF

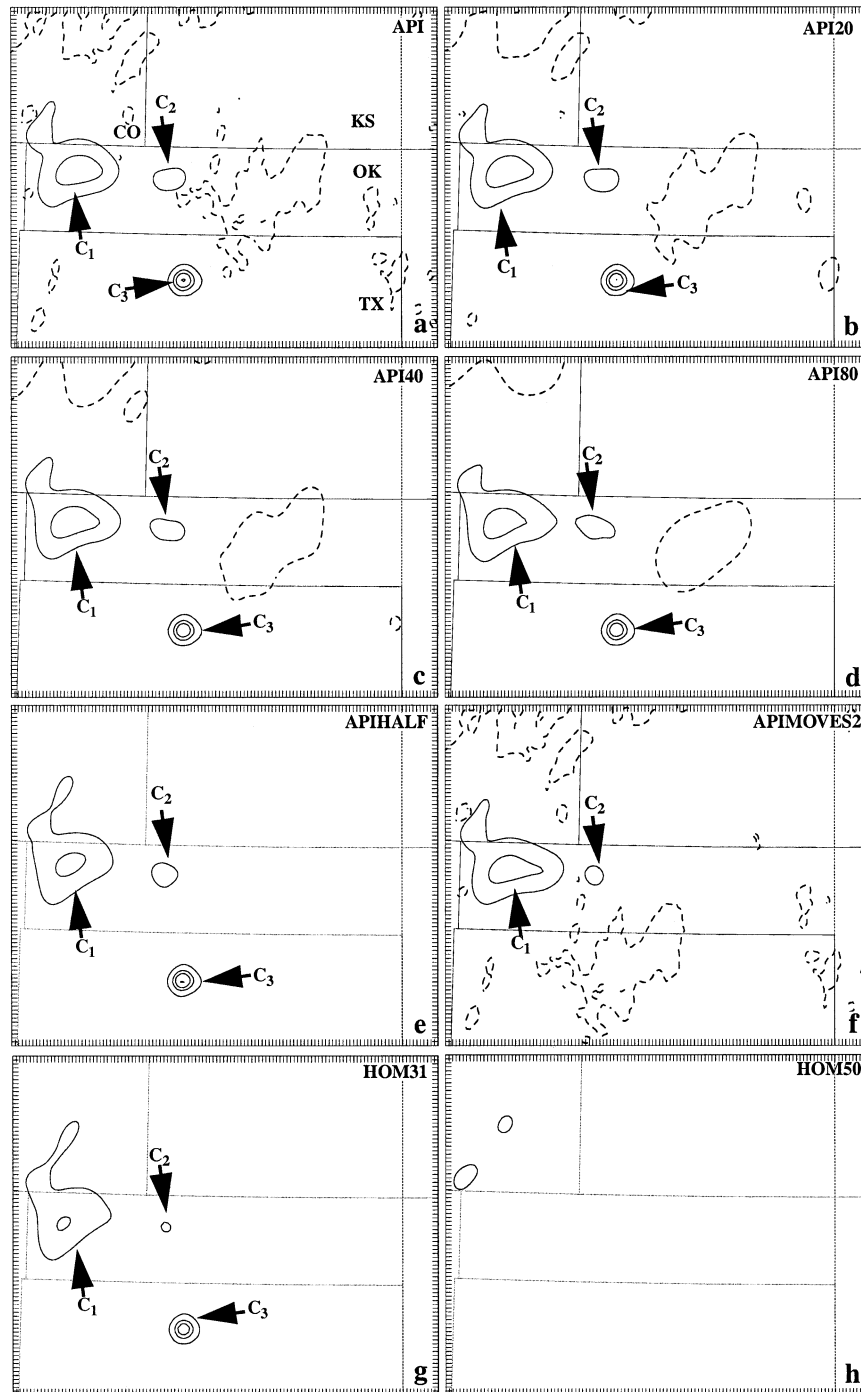


FIG. 14. RAMS grid 3 precipitation rate (at contour intervals of 1, 5, 10, 20, 40, 80, and 120 mm h^{-1}) at 26/1915 for expts (a) API, (b) API20, (c) API40, (d) API80, (e) APIHALF, (f) APIMOVES2, (g) HOM31, and (h) HOM50. Dashed contour represents initial volumetric soil moisture at 50% saturation.

(HOM50), and the rest of the experiments again fell somewhere in between. Although expt HOM50 had a colder surface temperature (≈ 4 K; not shown) than expt APIHALF because of a lower SSHF, expt HOM50 had the highest CAPE because of a compensating in-

crease in low-level humidity (Fig. 17c). On the other hand, although expt APIHALF had a warmer surface temperature than expt HOM50, the lower SLHF (hence reduced low-level humidity) resulted in a much lower value of CAPE. The other experiments fell somewhere

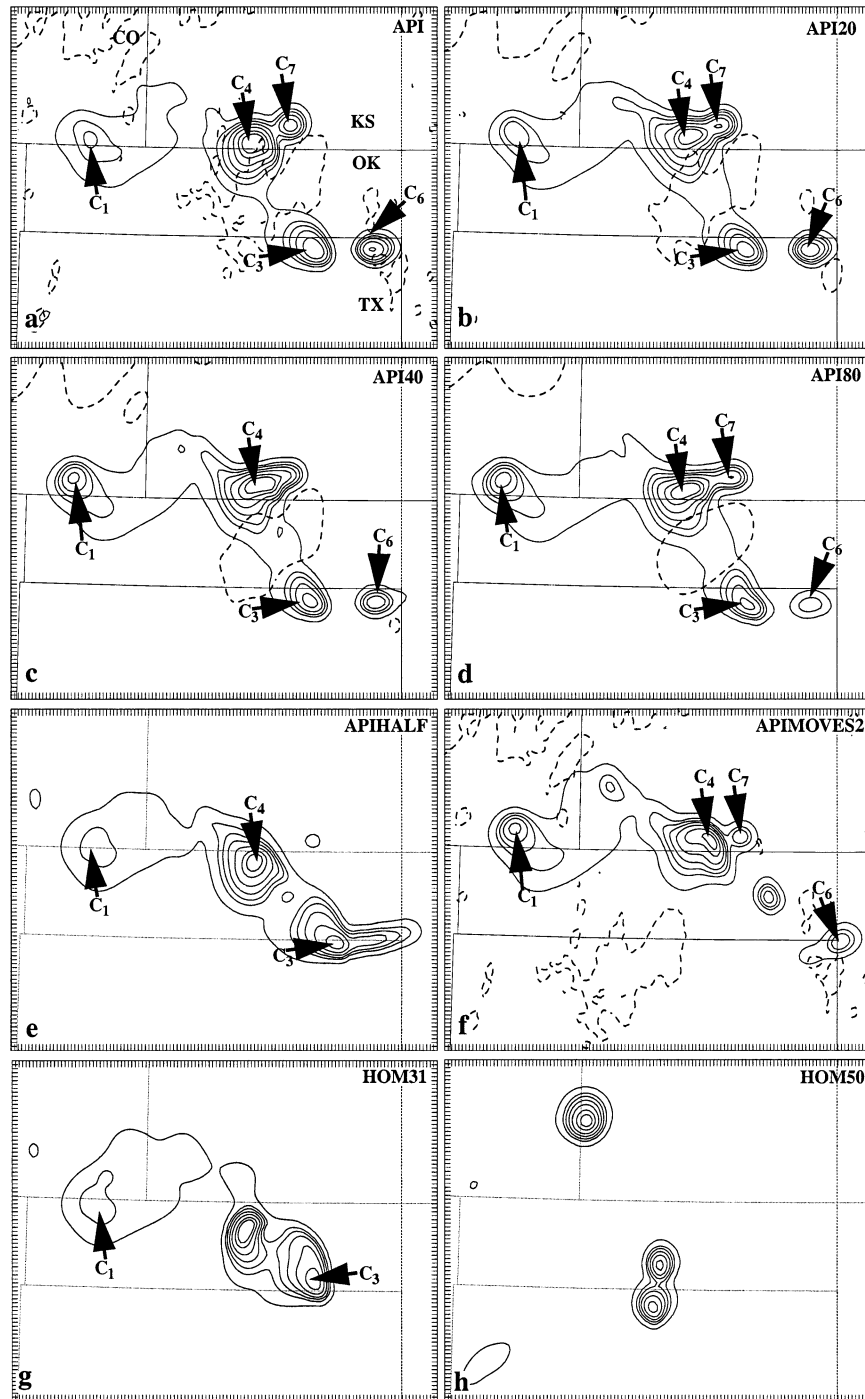


FIG. 15. As in Fig. 14, but for 26/2145.

in between the two extremes, but were closer to expt APIHALF.

In the grid 3 domain-averaged precipitation rate time series (Fig. 18a), expt HOM50 had the lowest precipitation rate among all the experiments, although it had the highest CAPE. Because of a higher SSHF in expts APIHALF and HOM31 (therefore warmer surface tem-

perature), the peak precipitation rate (hence peak convective activity) was reached 30 min sooner than expts API, API20, API40, and API80. Also, in general, expts APIMOVES2 and HOM31 had lower precipitation rates than expts API, API20, API40, and API80. In terms of the grid 3 domain-averaged accumulated precipitation time series, not surprisingly, expt HOM50 had the low-

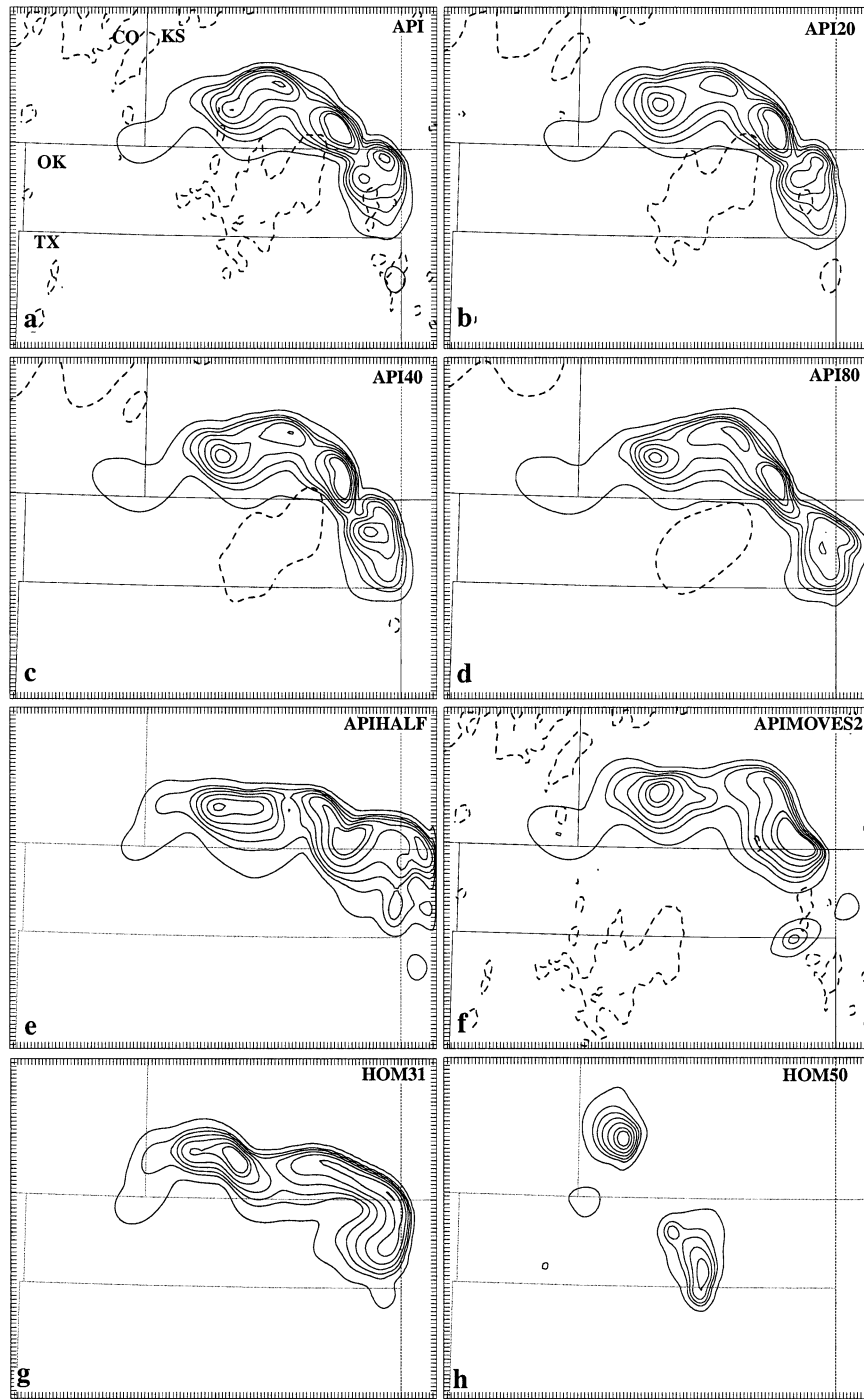


FIG. 16. As in Fig. 14, but for 26/2300.

est accumulated precipitation because of a delay in convection and precipitation being confined to limited areas of the domain. Expt APIHALF had almost 1 mm higher accumulated precipitation than expts API, API20, API40, API80, and HOM31 for about 30 min between 26/2300 and 26/2330. Because of the suppressed formation of C_3 in expt APIMOVES2, the accumulated

precipitation in expt APIMOVES2 was lower than those in expts API, API20, API40, and API80.

As an evaluation of the simulated accumulated precipitation, we compare the expt API 3-h accumulated precipitation in grid 3 with the data from the GCIP archive. There was little precipitation in the Texas panhandle in grid 3 (contrary to the 3-h accumulated pre-

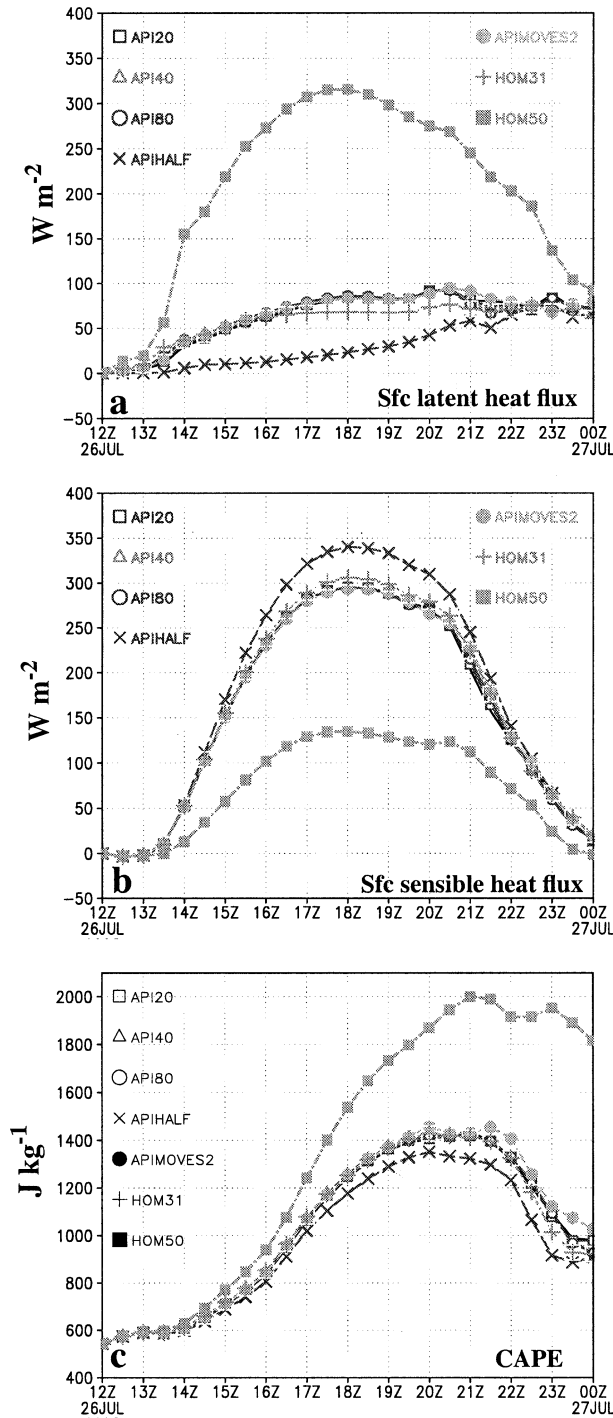


FIG. 17. Time series of grid 3 domain-averaged (a) surface latent heat flux ($W m^{-2}$); (b) surface sensible heat flux ($W m^{-2}$); and (c) CAPE ($J kg^{-1}$). Expt API is represented by the solid curve. Symbols for the other experiments are indicated.

precipitation from the GCIP archive in Fig. 19). As mentioned previously, the model did not capture the initiation of the convective line A_2 in the Texas panhandle and its subsequent development and northward advance-

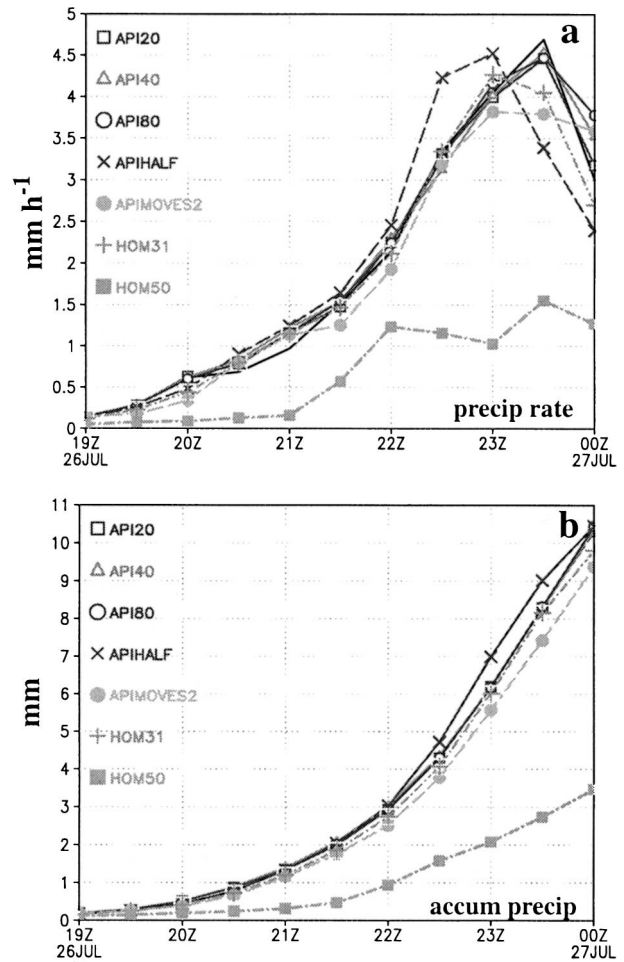


FIG. 18. Time series of grid 3 domain-averaged (a) precipitation rate ($mm h^{-1}$) and (b) accumulated precipitation (mm). Expt API is represented by the solid curve. Symbols for the other experiments are indicated.

ment (Fig. 1). Therefore, most of the convective precipitation was too far north into Kansas. The accumulated precipitation from other experiments also did not correspond exactly to observations. Nevertheless, RAMS reproduced some aspects of the observed MCS; that is, RAMS simulated a cloud shield of similar size and shape near the right place and time as compared to observations.

5. Discussion

In this study, the soil moisture distribution determined where convection was likely to occur. From the accumulated precipitation field (Fig. 19), as well as the precipitation rates (Figs. 14–16), it is clear that the NCMCs from the large soil moisture anomalies (e.g., S_2) tended to preferentially favor the convective cells to develop around their peripheries in this case. In other words, wetter soil contributes to a negative feedback in subsequent convective precipitation over the wetter soil. As

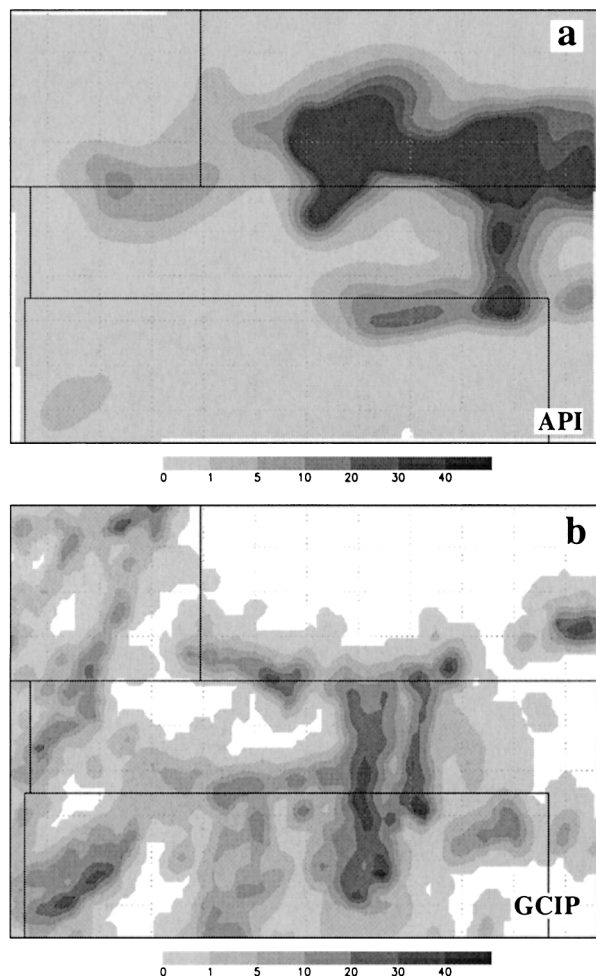


FIG. 19. The 3-h accumulated precipitation (mm) from 26/2100 to 27/0000 for (a) expt API and (b) 4-km GCIP precipitation database.

we have seen in expt APIMOVES2, wetter soil tends to suppress convection. Thus once the soil is wet, it is difficult for it to receive convective precipitation or initiate convection. In a two-dimensional (x - z) experiment (with a horizontal grid spacing of 2 km), Emori (1998) found that convection preferentially occurs on dry soil. Lynn et al. (1998) also found similar results as Emori in a 2D cumulus ensemble model. Although Emori and Lynn et al.'s results agreed with ours, a three-dimensional model would be needed to accurately represent the interaction of convection cells with the NCMCs induced by the soil moisture anomalies (e.g., the convective cells tracking along the periphery of S_2). As the MCS becomes more organized, with greater horizontal extent, we expect the NCMCs of the soil moisture anomalies to be less effective in influencing the development of the MCS.

Observational studies from Segal et al. (1989) and Rabin et al. (1990) also show that convection and cloudiness tend to be suppressed over regions of high latent

heat flux. In Segal et al.'s study, the temperature drop and moisture increase were observed up to 445 m AGL over irrigated areas. The maximum contrast between the irrigated areas and surroundings was on the order of 10 K. However, Segal et al. did not observe a sharply defined NCMC as anticipated because of the masking by the background flow. Rabin et al. investigated the influence of landscape variability in the initiation and development of cumulus clouds in Oklahoma. They observed that clouds formed the earliest over areas of high sensible heat flux, and cloud formation was suppressed over areas of high latent heat flux.

Our results from this case are in agreement with the observational studies of Segal et al. (1989) and Rabin et al. (1990) and the 2D modeling studies of Emori (1998) and Lynn et al. (1998) in demonstrating a negative feedback between convective precipitation and wet soil during the genesis phase of the MCS. However, under different atmospheric conditions, the feedback between convective precipitation and wet soil may be different. For example, in one 1999 case, the simulations were not sensitive to the soil moisture initialization because of the unstable atmospheric conditions (not shown). In a counterexample to the aforementioned case, Gallus and Segal (2000) found that convective precipitation was sensitive in a simulation (with CAPE over 5500 J kg^{-1} in some areas) to both the soil moisture and the CPS used. Gallus and Segal found that wetter soil generally produced a smaller precipitation maximum in the experiments with K-F CPS because the trigger function in the K-F CPS depends on the vertical velocity. In the experiments with the Betts-Miller-Janjic (BMJ; Betts and Miller 1986; Janjic 1994) CPS, wetter soil produced a larger precipitation maximum because the BMJ is sensitive to the low-level and mid-level humidity. Also, in the K-F CPS, the convergence of the parameterized downdrafts with the ambient flow over drier soil produced rainfall that was nonexistent in the experiments using the BMJ CPS due to the lack of parameterized downdrafts.

Using a one-dimensional model, Findell and Eltahir (2003a) determined the likelihood of convection as a function of the convective triggering potential (CTP) and the low-level humidity (HI_{low}) in the early morning sounding and the soil moisture condition. The CTP is computed from integrating the area between the environmental temperature profile and a moist adiabat drawn upward from the observed temperature 100 hPa above the surface to a point 300 hPa above the surface. The low-level humidity HI_{low} is the sum of the dewpoint depressions at 50 and 100 hPa above the surface. Several possibilities can occur depending on the initial early morning sounding: (i) deep convection is favored over dry soil (dry soil advantage); (ii) deep convection is favored over wet soil (wet soil advantage); and (iii) convection is atmospherically controlled (Fig. 20). Using the aforementioned definitions of CTP and HI_{low} , we found that the grid 3 average of CTP and HI_{low} to

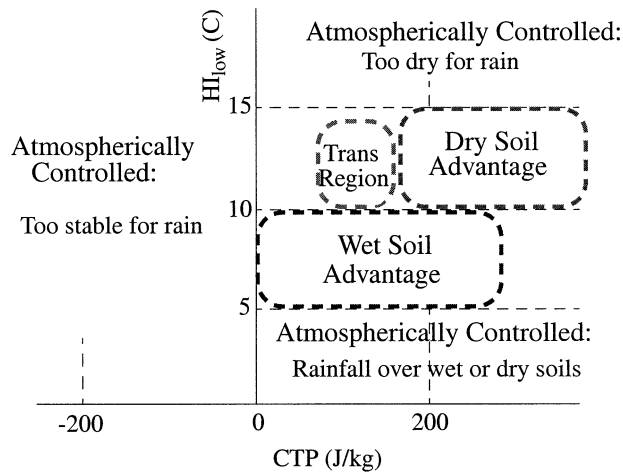


FIG. 20. The CTP– HI_{low} framework for describing atmospheric conditions in soil moisture–rainfall feedback [taken from Fig. 15 of Findell and Eltahir (2003a)].

be 250 J kg^{-1} and 15 K , respectively, at the model initial time. These values fall near the boundary between (i) deep convection favored over dry soil and (ii) deep convection unfavorable because of dry lower atmosphere (Fig. 20). Results from expts HOM31 and HOM50 (with homogeneous SMI)⁶ are not inconsistent with the theory from Findell and Eltahir (2003a), with convection being delayed and less widespread in grid 3 in expt HOM50 (wetter soil) as compared to expt HOM31 (drier soil) (Figs. 14, 15, and 16).

Using multiyear summer (June, July, and August) radiosonde data for the continental United States, Findell and Eltahir (2003b) computed the CTP and HI_{low} for various stations and classified the stations according to the various regimes in the CTP– HI_{low} space as in Findell and Eltahir (2003a). For example, Texas/Oklahoma panhandle falls within the regimes of (i) transition region between wet and dry soil advantage, (ii) atmospherically controlled region, and (iii) dry soil advantage. The Great Plains region, to the lee of the Rockies, falls within the regimes of (i) the transition region between wet and dry soil advantage and (ii) the atmospherically controlled region. To the east of the Great Plains, the region falls within the regime of wet soil advantage. The genesis phase of the simulated MCS (expts HOM31 and HOM50) in this case more or less falls under one of the categories determined by Findell and Eltahir (2003b) in the Texas/Oklahoma region: the category of dry soil advantage. Although interesting, it is beyond the scope of this paper to verify whether convection/soil moisture feedback behaves differently in different regions of the continental United States because of the different thermodynamic conditions. Earlier 1D model studies such

as Clark and Arritt (1995) and Segal et al. (1995) have also discovered the nonlinearity of the soil moisture atmosphere interaction. However, the conceptual model of Findell and Eltahir (2003a,b) provides a more unified picture of the soil moisture–atmosphere interaction.

The convective precipitation–soil moisture feedback mechanism [in our study as well as those of Emori (1998) and Lynn et al. (1998)] differs from the feedback of the large-scale flow and the soil moisture distribution. Namias (1959) was one of the first to suggest from observations that the soil moisture anomalies could assist in maintaining the persistence of large-scale atmospheric circulation anomalies and vice versa. An anomalous trough over a moist soil area prevents the buildup of an upper-level ridge, and regions of dry soil (as a result of drought) are associated with an anomalous upper-level ridge. Therefore, over the drier (moist) soil area, there would be reduced (increased) precipitation and maintenance of the dry (moist) soil conditions. Castelli and Rodriguez-Iturbe (1995) supported the finding of Namias (1959) using a semigeostrophic model. They found that when the warm–moist (cold–drying) precipitation anomaly of the baroclinic wave develops on top of a wetter (drier) soil, frontal collapse is reached sooner and the estimated precipitation greater.

Convection started at the same time in grid 3 for most of the experiments, and the morphology of the convective line was similar in most of the experiments. Even expt HOM31 (with homogeneous SMI at 31% saturation) produced results similar to those with heterogeneous SMI. Expt API80 (while still retaining soil moisture patches of approximately 40 km in horizontal scale) generated results very similar to those in expt API, albeit with weaker precipitation in some areas as compared to expt API. So, there is little gain in providing SMI finer than approximately 40 km in horizontal scale. This indicates the importance of large-scale dynamics. Some MCSs are weakly forced by their large-scale environments (e.g., Stensrud and Fritsch 1993), and we can only speculate that small-scale soil moisture anomalies would have a greater impact in those cases.

6. Conclusions

Using the API method to obtain soil moisture, we tested the sensitivity of varying the soil moisture initialization on the cloud-resolving grid (2.5-km horizontal grid spacing) of a real-data MCS simulation. Because of the severe drought in the Texas/Oklahoma panhandle, we had to lower the saturation API value in order to introduce heterogeneities in the soil moisture for the sensitivity experiments. The API soil moisture was exaggerated to test the maximum impact of the effects of the SMI. In the sensitivity experiments, we smoothed the initial soil moisture in the cloud-resolving grid with Barnes objective analysis, using a response amplitude of 0.5 and cutoff wavelengths of 20, 40, and 80 km. In addition, we also varied the soil moisture in amplitude

⁶ Since the theory of Findell and Eltahir (2003a) is based on a 1D model, a comparison with experiments using homogeneous SMI is more appropriate.

and displaced a soil moisture anomaly from its initial location. We also ran two experiments with homogeneous soil moisture initialization at 31% and 50% saturation. Except for expt HOM50, RAMS simulated a cloud shield, similar in location, timing, and size as compared to observations. However, the accumulated precipitation did not compare as well to observations. Our findings are summarized below.

- Smaller soil moisture anomalies are more easily smoothed out by the objective analysis filter. As a result, smaller soil moisture anomalies are not well represented in the smoothed soil moisture initialization (i.e., with cutoff wavelength of 80 km), which can lead to underestimating NCMCs and precipitation (associated with the NCMCs).
- In this simulation, the soil moisture distribution determined where convection was likely to occur. Wetter soil had a tendency to suppress convection. In addition, the NCMCs induced by the wet soil moisture anomalies provided a focusing mechanism for convection to develop along the peripheries of the wet soil moisture anomalies due to the enhanced vertical motion there. As a result, there existed a negative feedback between wet soil and convective precipitation. However, we expect the NCMCs to be less effective in influencing the development of the MCS as the MCS becomes more organized (i.e., larger in extent). Note that under certain atmospheric conditions, the negative feedback obtained here between wet soil and convection may not hold, as noted in other related studies discussed further in section 5.
- In this case, large-scale forcing, in the form of a quasi-stationary front, provided a favorable environment for convection to develop in this simulation. Thus, even expt HOM31 (with homogeneous SMI at 31% saturation) produced results similar to those with heterogeneous SMI. Also, expt API80 (while still retaining soil moisture patches of approximately 40 km in horizontal scale) had results very similar to those in expt API, albeit with weaker precipitation in some areas as compared to expt API. So, there is little gain in providing SMI finer than approximately 40 km in horizontal scale.

Acknowledgments. This research was funded by NOAA under Grant NA67RJ0152 Amend 34. The authors wish to thank Prof. Roger Pielke Sr. for suggesting the use of the NDVI dataset. The first author would also like to thank his Ph.D. committee members, Profs. Scott Denning, Paul Mielke, and Roger Pielke Sr. for their suggestions. We also thank Dr. Ken Mitchell and three anonymous reviewers for their helpful comments in improving this manuscript. Thanks go to Kevin Schaefer and Joe Eastman for their help in working with the NDVI data. The help from Chris Rozoff with L^AT_EX is much appreciated. Finally, we also thank Ray McAnnelly for processing the satellite data, Steve Sa-

leby for providing the code for the API calculation, and Brenda Thompson for proofreading and processing the manuscript, respectively. The NDVI dataset was provided by Brad Reed and Susan Maxwell of USGS, and the satellite data was provided by the Global Hydrology Resource Center.

APPENDIX

The Antecedent Precipitation Index

In this appendix, we present the algorithm for converting the API to volumetric soil moisture in grid 3. We used the EDAS soil moisture for grids 1 and 2. The volumetric soil moisture content (W) is the ratio of the volume of water (V_w) in the soil versus the total volume (V_t) of the soil:

$$W = \frac{V_w}{V_t}. \quad (\text{A1})$$

The API on the n th day is given by

$$(\text{API})_n = R_n + \kappa(\text{API})_{n-1}, \quad (\text{A2})$$

where the API value on the n th day depends on the rainfall accumulation on the n th day (R_n), the depletion coefficient (κ), and the API value on the $(n - 1)$ th day. The depletion coefficient (from Lee 1992) has a time dependence to account for the seasonality:

$$\kappa = 1 - 0.04 \left\{ \sin \left[2\pi \frac{(t - \tau_1 - \tau_2)}{\tau_0} \right] + 1 \right\}, \quad (\text{A3})$$

where t is the time in Julian days, τ_1 is 15 days, τ_2 is 91.25 days, and τ_0 is 365 days. The sinusoidal functional form of κ comes from Choudhury and Blanchard (1983). It is easy to see that the API on the n th day is the weighted sum of n days of rainfall accumulation, and κ normally ranges between 0.85 and 0.98 (Shaw 1994).

To compute the fractional soil moisture (w_{frac}), we use the following expression:

$$w_{\text{frac}} = \frac{\text{API}_n}{\text{API}_{\text{max}}}, \quad (\text{A4})$$

where API_{max} is the maximum API value possible. According to Chang and Wetzel (1991), the maximum API (centimeters) can be estimated by

$$\text{API}_{\text{max}} = (1 - \kappa)^{-1}. \quad (\text{A5})$$

Using Lee's (1992) formula for κ , the average κ for our study is 0.93. Using the above equation from Chang and Wetzel (1991) and a κ of 0.93, the maximum API is 140 mm. Because of the dry soil conditions, we lowered API_{max} to 40 mm because we wanted to introduce heterogeneities in the SMI. Despite the artificial introduction of moist soil anomalies, the grid 3 soil moisture for expt API remained quite dry, with a domain-averaged value of only 31% saturation. Luo et al. (2003)

found the lowest mean volumetric soil moisture in the 0–40-cm layer during the May–July 1998 drought in Oklahoma to be about 50% saturation. Thus, this artificial increase in soil moisture is not that unrealistic, at least in the domain-averaged sense. The API method is better at estimating near soil moisture rather than deep-layer soil moisture. As discussed in section 3b, we assumed the initial soil moisture to be invariant with depth.

We performed two 15-h simulations in which the grid 3 soil moisture deeper than 0.52 m in expt API (see Table 2) was increased by 20% and 40%, respectively, while keeping the maximum soil moisture at 100% saturation. However, we found that two aforementioned experiments did not differ substantially from expt API. So, the assumption of constant soil moisture with depth in grid 3 did not have a large impact on the simulations.

Note that the soil-type dataset has not yet been implemented in RAMS. We chose sandy clay loam as the single soil type for the entire model because it has an intermediate texture as compared to the soil types in the central United States (see Foth and Schafer 1980; Fast and McCorcle 1991).

To calculate the volumetric soil moisture, we multiply w_{frac} by the saturation volumetric moisture content ($0.42 \text{ m}^3 \text{ m}^{-3}$) for the sandy clay loam soil type. In saturated soil, all the pore spaces in the soil are occupied, and the soil cannot hold additional water (Shaw 1994). We constrained the minimum volumetric soil moisture to a value of $0.1 \text{ m}^3 \text{ m}^{-3}$ when converting the API to volumetric soil moisture. This minimum soil moisture value is within the minimum range in the Oklahoma Mesonet. We interpolated the soil moisture to grid 3 by using a bicubic spline interpolation (Vetterling et al. 1992).

REFERENCES

- Ashby, C. T., W. R. Cotton, and R. McAnelly, 2001: Impact of soil moisture initialization on a simulated flash flood. Preprints, *15th Conf. on Precipitation Extremes: Prediction, Impacts, and Responses*, Albuquerque, NM, Amer. Meteor. Soc., 260–263.
- Avissar, R., and R. A. Pielke, 1991: The impact of plant stomatal control on mesoscale atmospheric circulations. *Agric. For. Meteorol.*, **54**, 353–372.
- Barnes, S. L., 1964: A technique for maximizing details in numerical weather map analysis. *J. Appl. Meteorol.*, **3**, 396–409.
- Basara, J. B., D. S. Arndt, H. L. Johnson, J. G. Brotzge, and K. C. Crawford, 1999: An analysis of the drought of 1998 using the Oklahoma Mesonet. *Eos, Trans. Amer. Geophys. Union*, **79**, 258.
- Bell, G. D., and J. E. Janowiak, 1995: Atmospheric circulation associated with the Midwest floods of 1993. *Bull. Amer. Meteor. Soc.*, **76**, 681–696.
- , M. S. Halpert, C. F. Ropelewski, V. E. Kousky, A. V. Douglas, R. C. Schnell, and M. E. Gelman, 1999: Climate assessment for 1998. *Bull. Amer. Meteor. Soc.*, **80**, S1–S48.
- Bernardet, L. R., and W. R. Cotton, 1998: Multiscale evolution of a derecho-producing mesoscale convective system. *Mon. Wea. Rev.*, **126**, 2991–3015.
- , L. D. Grasso, J. E. Nachamkin, C. A. Finley, and W. R. Cotton, 2000: Simulating convective events using a high-resolution mesoscale model. *J. Geophys. Res.*, **105**, 14 963–14 982.
- Betts, A. K., and M. J. Miller, 1986: A new convective adjustment scheme. Part II: Single column tests using GATE wave, BOMEX, and arctic air-mass data sets. *Quart. J. Roy. Meteor. Soc.*, **112**, 693–709.
- Carlson, T. N., and D. A. Ripley, 1997: On the relation between NDVI, fractional vegetation cover, and leaf area index. *Remote Sens. Environ.*, **62**, 241–252.
- Castelli, F., and I. Rodriguez-Iturbe, 1995: Soil moisture–atmosphere interaction in a moist semigeostrophic model of baroclinic instability. *J. Atmos. Sci.*, **52**, 2152–2159.
- Chang, J.-T., and P. J. Wetzel, 1991: Effects of spatial variations of soil moisture and vegetation on the evolution of a prestorm environment: A numerical case study. *Mon. Wea. Rev.*, **119**, 1368–1390.
- Chen, F., and R. Avissar, 1994a: The impact of land-surface wetness heterogeneity on mesoscale heat fluxes. *J. Appl. Meteorol.*, **33**, 1323–1340.
- , and —, 1994b: Impact of land-surface moisture variability on local shallow convective cumulus and precipitation in large-scale models. *J. Appl. Meteorol.*, **33**, 1382–1401.
- , R. A. Pielke Sr., and K. Mitchell, 2001a: Development and application of land-surface models for mesoscale atmospheric models: Problems and promises. *Observations and Modeling of the Land-Surface Hydrological Processes*, V. Lakshmi, J. Alberston, and J. Schaak, Eds., Amer. Geophys. Union, 107–135.
- , T. T. Warner, and K. Manning, 2001b: Sensitivity of orographic moist convection to landscape variability: A study of the Buffalo Creek, Colorado, flash flood case of 1996. *J. Atmos. Sci.*, **58**, 3204–3223.
- Choudhury, B. J., and B. J. Blanchard, 1983: Simulating soil water recession coefficients for agricultural water sheds. *Water Resour. Bull.*, **19**, 241–247.
- Clark, C. A., and R. W. Arritt, 1995: Numerical simulations of the effect of soil moisture and vegetation cover on the development of deep convection. *J. Appl. Meteorol.*, **34**, 2029–2045.
- Cotton, W. R., and R. A. Anthes, 1989: *Storm and Cloud Dynamics*. Academic Press, 883 pp.
- , R. L. George, P. J. Wetzel, and R. L. McAnelly, 1983: A long-lived mesoscale convective complex. Part I: Mountain-generated component. *Mon. Wea. Rev.*, **111**, 1893–1918.
- , M.-S. Lin, R. L. McAnelly, and C. J. Trembeck, 1989: A composite model of mesoscale convective complexes. *Mon. Wea. Rev.*, **117**, 765–783.
- , and Coauthors, 2003: RAMS 2001: Current status and future directions. *Meteor. Atmos. Phys.*, **82**, 5–29.
- Dalu, G. A., and R. A. Pielke, 1993: Vertical heat fluxes generated by mesoscale atmospheric flow induced by thermal inhomogeneities in the PBL. *J. Atmos. Sci.*, **50**, 919–926.
- , —, R. Avissar, G. Kallos, M. Baldi, and A. Guerrini, 1991: Linear impact of thermal inhomogeneities on mesoscale atmospheric flow with zero synoptic wind. *Ann. Geophys.*, **9**, 641–647.
- Dirmeyer, P. A., 1995: Problems in initializing soil wetness. *Bull. Amer. Meteor. Soc.*, **76**, 2234–2240.
- , and J. Shukla, 1993: Observational and modeling studies of the influence of soil moisture anomalies on the atmospheric circulation. *Predictions of Interannual Climate Variations*, J. Shukla, Ed., NATO ASI Series I, Vol. 6, Springer-Verlag, 1–23.
- EK, M. B., K. E. Mitchell, Y. Lin, P. Grunmann, E. Rogers, G. Gayno, and V. Koren, 2003: Implementation of the upgraded Noah land-surface model in the NCEP operational mesoscale Eta Model. *J. Geophys. Res.*, **108**, 8851, doi:10.1029/2002JD003296.
- Emori, S., 1998: The interaction of cumulus convection with soil moisture distribution: An idealized simulation. *J. Geophys. Res.*, **103** (D8), 8873–8884.
- Entekhabi, D., I. Rodriguez-Iturbe, and F. Castelli, 1996: Mutual interaction of soil moisture state and atmospheric processes. *J. Hydrol.*, **184**, 3–17.
- Fast, J. D., and M. D. McCorcle, 1991: The effect of heterogeneous soil moisture on a summer baroclinic circulation in the central United States. *Mon. Wea. Rev.*, **119**, 2140–2167.

- Findell, K. L., and E. A. B. Eltahir, 2003a: Atmospheric controls on soil moisture–boundary layer interactions. Part I: Framework development. *J. Hydrometeorol.*, **4**, 552–569.
- , and —, 2003b: Atmospheric controls on soil moisture–boundary layer interactions. Part II: Feedbacks within the continental United States. *J. Hydrometeorol.*, **4**, 570–583.
- Foth, H. D., and J. W. Schafer, 1980: *Soil Geography and Land Use*. John Wiley and Sons, 484 pp.
- Fritsch, J. M., R. J. Kane, and C. R. Chelius, 1986: Contribution of mesoscale convective weather systems to the warm-season precipitation in the United States. *J. Climate Appl. Meteorol.*, **25**, 1333–1345.
- Gallus, W. A., and M. Segal, 2000: Sensitivity of forecast rainfall in a Texas convective system to soil moisture and convective parameterization. *Wea. Forecasting*, **15**, 509–525.
- , and —, 2001: Impact of improved initialization of mesoscale features on convective system rainfall in 10-km Eta simulations. *Wea. Forecasting*, **16**, 680–696.
- Golaz, J.-C., H. Jiang, and W. R. Cotton, 2001: A large-eddy simulation study of cumulus clouds over land and sensitivity to soil moisture. *Atmos. Res.*, **59–60**, 373–392.
- Grasso, L. D., 2000: A numerical simulation of dryline sensitivity to soil moisture. *Mon. Wea. Rev.*, **128**, 2816–2834.
- Harrington, J. Y., 1997: The effects of radiative and microphysical processes on simulated warm and transition-season arctic stratus. Ph.D. dissertation, Colorado State University, 289 pp.
- , M. P. Meyers, R. L. Walko, and W. R. Cotton, 1995: Parameterization of ice crystal conversion processes due to vapor deposition for mesoscale models using double-moment basis functions. *J. Atmos. Sci.*, **52**, 4344–4366.
- , T. Reisin, W. R. Cotton, and S. M. Kreidenweis, 1999: Cloud resolving simulations of Arctic stratus. Part II: Transition-season clouds. *Atmos. Res.*, **51**, 45–75.
- Hong, S.-Y., and E. Kalnay, 2002: The 1998 Oklahoma–Texas drought: Mechanistic experiments with NCEP global and regional models. *J. Climate*, **15**, 945–963.
- Janjic, Z. I., 1994: The step-mountain eta coordinate model: Further development of the convection, viscous sublayer, and turbulence closure model schemes. *Mon. Wea. Rev.*, **122**, 928–945.
- Johnson, R. H., and P. J. Hamilton, 1988: The relationship of surface pressure features to the precipitation and air flow structure of an intense midlatitude squall line. *Mon. Wea. Rev.*, **116**, 1444–1472.
- Kain, J. S., and J. M. Fritsch, 1990: A one-dimensional entraining/detraining plume model and its application in convective parameterization. *J. Atmos. Sci.*, **47**, 2784–2802.
- , and —, 1998: Multiscale convective overturning in mesoscale convective systems: Reconciling observations, simulations, and theory. *Mon. Wea. Rev.*, **126**, 2254–2273.
- Kunkel, K. E., S. A. Changnon, and J. R. Angel, 1994: Climatic aspects of the 1993 Mississippi River basin flood. *Bull. Amer. Meteor. Soc.*, **75**, 811–822.
- Kuo, S. L., 1974: Further studies of the parameterization of the effect of cumulus convection on large-scale flow. *J. Atmos. Sci.*, **31**, 1232–1240.
- Lee, T. J., 1992: The impact of vegetation on the atmospheric boundary layer and convective storms. Ph.D. dissertation, Colorado State University, 137 pp.
- Liu, Y., and R. Avissar, 1999: A study of persistence in the land–atmosphere system using a general circulation model and observations. *J. Climate*, **12**, 2139–2153.
- Luo, L., and Coauthors, 2003: Validation of the North American Land Data Assimilation System (NLDAS) retrospective forcing over the Southern Great Plains. *J. Geophys. Res.*, **108**, 8843, doi:10.1029/2002JD003246.
- Lynn, B. H., W.-K. Tao, and P. J. Wetzel, 1998: A study of landscape-generated deep moist convection. *Mon. Wea. Rev.*, **126**, 928–942.
- Maddox, R. A., 1980: Mesoscale convective complexes. *Bull. Amer. Meteor. Soc.*, **61**, 1374–1387.
- McAnelly, R. L., J. E. Nachamkin, W. R. Cotton, and M. E. Nicholls, 1997: Upscale evolution of MCSs: Doppler radar analysis and analytical investigation. *Mon. Wea. Rev.*, **125**, 1083–1110.
- Meyers, M. P., R. L. Walko, J. Y. Harrington, and W. R. Cotton, 1997: New RAMS cloud microphysics parameterization. Part II: The two-moment scheme. *Atmos. Res.*, **45**, 3–39.
- Nachamkin, J. E., and W. R. Cotton, 2000: Interactions between a developing mesoscale convective system and its environment. Part II: Numerical simulation. *Mon. Wea. Rev.*, **128**, 1225–1244.
- Namias, J., 1959: Persistence of mid-tropospheric circulations between adjacent months and seasons. *The Atmosphere and the Sea in Motion*, B. Bolin, Ed., Rockefeller Institute Press, 240–248.
- Njoku, E., and D. Entekhabi, 1996: Passive microwave remote sensing of soil moisture. *J. Hydrol.*, **184**, 101–129.
- Olsson, P. Q., and W. R. Cotton, 1997: Balanced and unbalanced circulations in a primitive equation simulation of a midlatitude MCC. Part I: The numerical simulation. *J. Atmos. Sci.*, **54**, 457–478.
- Pielke, R. A., 2001: Influence of the spatial distribution of vegetation and soils on the prediction of cumulus convective rainfall. *Rev. Geophys.*, **39**, 151–177.
- , and M. Segal, 1986: Mesoscale circulations forced by differential terrain heating. *Mesoscale Meteorology and Forecasting*, P. S. Ray, Ed., Amer. Meteor. Soc., 516–548.
- , T. J. Lee, J. H. Copeland, J. L. Eastman, C. L. Ziegler, and C. A. Finley, 1997: Use of USGS-provided data to improve weather and climate simulations. *Ecol. Appl.*, **7**, 3–21.
- , G. E. Liston, J. L. Eastman, L. Lu, and M. Coughenour, 1999: Seasonal weather prediction as an initial value problem. *J. Geophys. Res.*, **104**, 19 463–19 479.
- Rabin, R. M., S. Stadler, P. J. Webster, D. J. Stensrud, and M. Gregory, 1990: Observed effects of landscape variability on convective clouds. *Bull. Amer. Meteor. Soc.*, **71**, 272–280.
- Segal, M., and R. W. Arritt, 1992: Nonclassical mesoscale circulations caused by surface sensible heat-flux gradients. *Bull. Amer. Meteor. Soc.*, **73**, 1593–1604.
- , R. Avissar, M. C. McComber, and R. A. Pielke, 1988: Evaluation of vegetation effects on the generation and modification of mesoscale circulations. *J. Atmos. Sci.*, **45**, 2268–2292.
- , W. Schreiber, G. Kallos, R. A. Pielke, J. R. Garratt, J. Weaver, A. Rodi, and J. Wilson, 1989: The impact of crop areas in northeast Colorado in midsummer mesoscale thermal circulations. *Mon. Wea. Rev.*, **117**, 809–825.
- , R. W. Arritt, C. Clark, R. Rabin, and J. Brown, 1995: Scaling evaluation of the effect of surface characteristics on potential for deep convection over uniform terrain. *Mon. Wea. Rev.*, **123**, 383–400.
- Sellers, P. J., C. J. Tucker, G. J. Collatz, S. O. Los, C. O. Justice, D. A. Dazlich, and D. A. Randall, 1994: A global 1 degree by 1 degree NDVI data set for climate studies. Part 2: The generation of global fields of terrestrial biophysical parameters from the NDVI. *Int. J. Remote Sens.*, **15**, 3519–3545.
- Shaw, E. M., 1994: *Hydrology in Practice*. 3d ed. Chapman and Hall, 569 pp.
- Stensrud, D. J., and J. M. Fritsch, 1993: Mesoscale convective systems in weakly forced large-scale environments. Part I: Observations. *Mon. Wea. Rev.*, **121**, 3326–3344.
- Tripoli, G. J., and W. R. Cotton, 1982: The Colorado State University Three-Dimensional Cloud/Mesoscale Model. Part I: General theoretical framework and sensitivity experiments. *Atmos. Res.*, **18**, 185–219.
- Vetterling, W. T., S. A. Teukolsky, and W. H. Press, 1992: *Numerical Recipes: Example Book (FORTRAN)*. Cambridge University Press, 245 pp.
- Walko, R. L., and Coauthors, 2000: Coupled atmosphere–biophysics–hydrology models for environmental modeling. *J. Appl. Meteorol.*, **39**, 931–944.
- Warner, T. T., and H. M. Hsu, 2000: Nested-model simulation of moist convection: The impact of coarse-grid parameterized convection

- on fine-grid resolved convection. *Mon. Wea. Rev.*, **128**, 2211–2231.
- Weisman, M. L., W. C. Skamarock, and J. B. Klemp, 1997: The resolution dependence of explicitly modeled convective systems. *Mon. Wea. Rev.*, **125**, 527–548.
- Wetzel, P. J., W. R. Cotton, and R. L. McAnelly, 1983: A long-lived mesoscale convective complex. Part II: Evolution and structure of the mature complex. *Mon. Wea. Rev.*, **111**, 1919–1937.
- Yan, H., and R. A. Anthes, 1988: The effects of variations in surface moisture on mesoscale circulations. *Mon. Wea. Rev.*, **116**, 192–208.
- Yang, R., M. J. Fennessy, and J. Shukla, 1994: The influence of initial soil wetness on medium-range surface weather forecasts. *Mon. Wea. Rev.*, **122**, 471–485.
- Zhang, D.-L., K. Gao, and D. B. Parsons, 1989: Numerical simulation of an intense squall line during 10–11 June 1985 PRE-STORM. Part I: Model verification. *Mon. Wea. Rev.*, **117**, 960–994.
- Zipser, E. J., 1982: Use of a conceptual model of the life cycle of mesoscale convective systems to improve very-short-range forecasts. *Nowcasting*, K. Browning, Ed., Academic Press, 191–204.